



1 **Springtime aerosol load as observed from ground-based and** 2 **airborne lidars over Northern Norway**

3 Patrick Chazette¹, Jean-Christophe Raut², and Julien Totems¹

4 ¹Laboratoire des Sciences du Climat et de l'Environnement (LSCE), Laboratoire mixte CEA-CNRS-UVSQ, UMR
5 1572, CEA Saclay, 91191 Gif-sur-Yvette, France

6 ²LATMOS/IPSL, Sorbonne Université, CNRS, UVSQ, Paris, France

7 *Correspondence to:* Patrick Chazette (patrick.chazette@lsce.ipsl.fr)

8 **Abstract.** To investigate the origin of springtime aerosols in the Arctic region we performed ground-based and
9 airborne 355 nm-Raman lidar observations in the North of Norway (Hammerfest). Two lidars were embedded (i)
10 on an ultra-light aircraft for vertical (nadir) or horizontal line-of-sight measurements, (ii) in an air-conditioned van
11 on the ground for vertical (zenith) measurements. This field experiment was designed as part of the Pollution in
12 the ARCTic System (PARCS) project of the French Arctic initiative, and took place from 13 to 26 May, 2016. The
13 consistency between lidar measurements is verified by comparing nadir, horizontal line-of-sight, and ground-based
14 Raman lidar profiles. Dispersion of the order of 0.01 km⁻¹ is obtained between lidar-derived aerosol extinction
15 coefficients at 355 nm. The aerosol load measured in the three first kilometers of the troposphere remains low
16 throughout the campaign, with aerosol optical thickness (AOT) \lesssim 0.1 at 355 nm (\sim 0.05 at 550 nm). The main
17 contributors to the evolution of the aerosol load at low altitude prove to be one of the flares of the nearby Melkoya
18 gas processing facility, the oceanic source and the transport of aerosols from industrial sites in Russia. Moreover,
19 ground-based lidar measurements allowed the possibility to identify three cases of long-range aerosol transport
20 (between 3 and 8 km above the mean sea level). Using back trajectories computed with the Lagrangian model
21 FLEXPART-WRF, these aerosol plumes are shown to be the result of the strong forest fires that occurred in the
22 area of Fort McMurray, in Canada. They can, at most double the AOT value over the Arctic area, with an anomaly
23 of 0.1 on the AOT at 355 nm.

24 **Keywords:** PARCS, Raman, lidar, ULA, airborne, aerosol, optical properties, back trajectories
25

26 **1 Introduction**

27 The pristine Arctic environment is very sensitive and can be easily disturbed by anthropogenic activities, with
28 irreparable consequences. Anthropogenic aerosols play a major role in the evolution of the Arctic radiative balance,
29 as pointed out by the IPCC (IPCC, 2014), and have to be better quantified. Moreover, the Arctic region is exposed
30 to thin but persistent haze (Breider et al., 2014; Shaw, 1995), as well as episodic events of carbonaceous aerosol
31 plumes in the free troposphere (Brock et al., 2011; Quinn et al., 2008; Warneke et al., 2010) since the industrial
32 era. This environmental challenge posed by tropospheric aerosols in the Arctic has already been pointed out by
33 Barrie (1986) and, even more recently by authors as Law et al. (2017) or Yang et al. (2014), who analyzed the
34 climatic impact and showed that aerosols induce a warming of about 0.6 K decade⁻¹.

35 Following these observations, the French Arctic initiative project Pollution in the ARCTic System (PARCS) was
36 performed to improve our understanding of aerosols in the Arctic troposphere. A point of focus was the long-range



37 transport of anthropogenic and biomass burning aerosols over the Arctic region. This innovative field campaign
38 took place from 13 to 26 May, 2016 in the region of Hammerfest (70°39'45"N 23°41'00"E, Norway), 90 km
39 southwest of the North Cape, within the Arctic Circle. It involved ground-based and airborne Raman lidar
40 observations. The mesoscale dynamic modeling was performed using the Weather Research and Forecasting
41 (WRF) model (Skamarock et al., 2008).

42 The PARCS experiment follows several international initiatives such as the recent Arctic Climate Change,
43 Economy and Society (ACCESS) over Northern Norway in July 2012 (Raut et al., 2017). ACCESS itself followed
44 the international Polar Study initiatives using Aircraft, Remote Sensing, Surface Measurements and Models,
45 Climate, Chemistry, Aerosols and Transport (POLARCAT) in 2008 (Ancellet et al., 2014), and the Arctic Research
46 of the Composition of the Troposphere from Aircraft and Satellites (ARCTAS) in 2008 (Jacob et al., 2009).

47 Obviously, the PARCS experiment is a snapshot of the aerosol situation in Northern Norway. As in all field
48 campaigns, the atmospheric environment is sampled over a short period of time and is not necessarily
49 representative of the local and seasonal meteorological conditions. The PARCS experiment took place during
50 large-scale weather conditions disturbed by the strong El Niño of 2015-2016 (Hu and Fedorov, 2017), which led
51 to temperatures in the Arctic planetary boundary layer (PBL) 3 to 4 °C above the 10-year normal climatic
52 conditions. Also associated with such exceptional atmospheric conditions, transport in the high troposphere
53 favored the presence of air masses from North America. Spring 2016 was marked by extreme wildfires in Canada's
54 Alberta territory, close to Fort McMurray (Kochtubajda et al., 2017; Landis et al., 2018). The coupling between
55 pyro-convection (Fromm et al., 2005; Peterson et al., 2015) and large-scale atmospheric transport may inject large
56 quantities of aerosols into the upper troposphere (Ancellet et al., 2016), whose lifetime greatly exceeds a week in
57 the absence of precipitation throughout their transport. Part of these aerosol layers were sampled by a ground-
58 based Raman lidar, which made it possible to describe both the vertical structure and the optical properties of the
59 aerosol plumes (Chazette et al., 2014), but also the history of their transport using the synergy between the Cloud-
60 Aerosol Lidar with Orthogonal Polarization (CALIOP) (Winker et al., 2003), the Moderate Resolution Imaging
61 Spectroradiometer (MODIS) (King et al., 1992) spaceborne instruments, and mesoscale modeling. The observation
62 of biomass fire aerosol transported at high altitude over long distances has already been reported by several authors
63 for different regions of the Earth (Ancellet et al., 2016; Formenti et al., 2002; Forster et al., 2001; Paris et al., 2009;
64 Quennehen et al., 2011; Sitnov and Mokhov, 2017). During the POLARCAT summer campaign in 2008, (Schmale
65 et al., 2011) and (Thomas et al., 2013) characterized aerosol and gas pollution from fire plumes transported from
66 North America to Greenland. Franklin et al. (2014) and Taylor et al. (2014) documented a case study of aerosol
67 removal in a biomass burning plume over eastern Canada in 2011. More recently, the long-range transport of
68 aerosols from Siberia has also already been evidenced (Marelle et al., 2015; Sitnov and Mokhov, 2017). During
69 the ACCESS airborne campaign in summer 2012 (Roiger et al., 2015), extensive boreal forest fires resulted in
70 significant aerosol transport to the Arctic (Raut et al., 2017). These plumes originating from Siberian wildfires are
71 very common during late spring and summer, and they may be mixed with aerosols coming from highly polluting
72 industrial sources such as oil and gas rigs, or petroleum refineries. Vaughan et al. (2018) describe the transport of
73 biomass burning aerosols over the United Kingdom originating from extensive and intense forest fires over Canada
74 in spring 2016. It should be noted that all previous authors only reported isolated long-distance transport events
75 and that this type of phenomenon is rare; the probability to observe one during the short duration of the PARCS

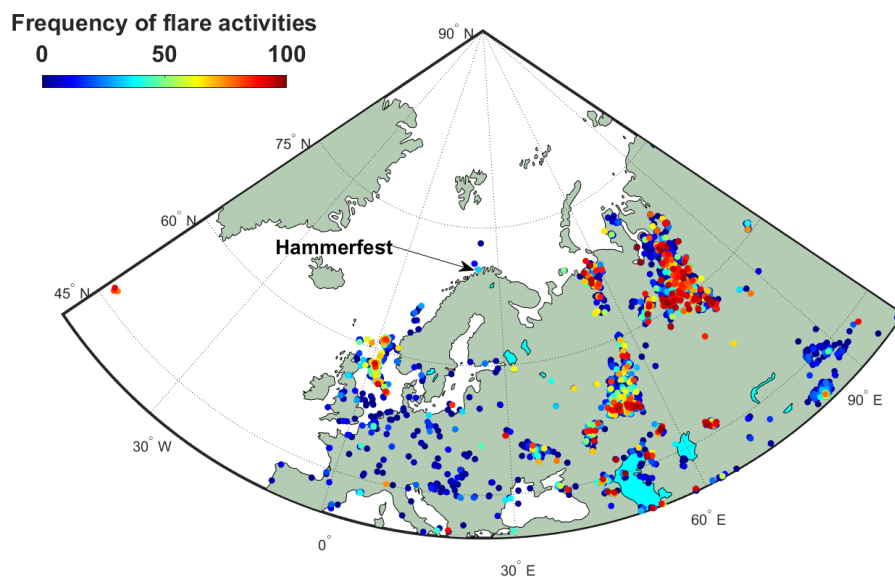


76 campaign was low. The chosen period for PARCS associated with a strong El Niño certainly favored long-range
77 transport of aerosols and offered an opportunity to sample 3 different tropospheric plumes.
78 This paper focuses on the long-range transported aerosols observed during the PARCS campaign as well as the
79 evolution of the aerosol load in the low troposphere. The field experiment is presented in Section 2, where ground-
80 based and airborne measurements are described. The large-scale observations derived from spaceborne
81 instruments and mesoscale modeling are presented in Section 3. Section 4 is devoted to the description of the
82 aerosol structures observed during the field campaign, with a spotlight on the low troposphere. Section 5 is
83 dedicated to the identification of the origins of the high-altitude aerosol plumes. The data coherence is discussed
84 in Section 6 and the conclusion is presented in Section 7.

85 2 Field experiment

86 The aerosol load is investigated using observations gathered from 13 to 26 May, 2016, during the PARCS field
87 campaign held in Northern Norway, over 70°N (Figure 1). The ground-based van MAS (Mobile Atmospheric
88 Station (Raut and Chazette, 2009)) and an ultra-light aircraft (ULA) were mainly equipped with active remote
89 sensing instruments (Figure 2): the Weather Atmospheric Lidar (WALI) and the Lidar for Automatic Atmospheric
90 Survey Using Raman Scattering (LAASURS), respectively.

91 We selected an experimental site near Hammerfest, next to the airport. The main reason for this is that the Melkoya
92 gas processing facility, which is the northernmost coastal installation and uses the latest techniques of LNG
93 (Liquefied Natural Gas), has two potentially active flares that could significantly influence atmospheric aerosol
94 concentrations: a high-pressure flare from processing and a low-pressure flare from loading and storing LNG. In
95 addition, with the local and shipping activities, the region may be subject to the advection of air masses from the
96 Murmansk area, which has a large concentration of oil and gas industries. We benefited from the help of the Avinor
97 crew of Hammerfest Airport in order to have a suitable operating base and all the necessary power supply. They
98 also helped us navigate the ULA, freely lent their hangar on the airport and offered staff support.



99

100 **Figure 1: Location of the ground-based measurement site, close to Hammerfest (Norway). The frequencies of the main**
101 **flares activities for both oil and gas rigs are given following (Elvidge et al., 2016) for 2016.**

102



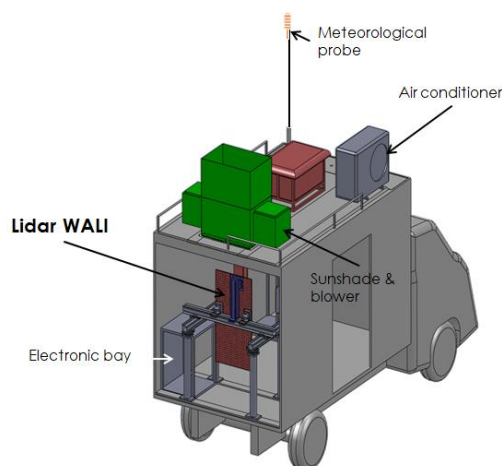
103

104 **Figure 2: Left picture: Mobile atmospheric station (MAS) located near the Hammerfest airport, equipped with the**
105 **WALI Raman lidar. Right picture: N₂-Raman lidar LAASURS embedded on a ULA. The ULA is flying over the**
106 **Melkoya platform where a gas flaring is active.**

107 2.1 Ground-based measurements

108 Figure 2 shows the MAS, located close to the Hammerfest airport. A schematic representation of the MAS and its
109 onboard instruments is given in Figure 3. It was equipped with the 354.7 nm water vapor Raman lidar WALI
110 (Chazette et al., 2014). These instruments carried out continuous measurements from 13 to 26 May, 2016, with a
111 final vertical resolution of 15 m and 1-minute integration (~1000 laser shots). The main characteristics of WALI
112 are summarized in Table 1.

113



114
 115 **Figure 3: Schematic representation of the MAS equipped with the Raman lidar WALI.**

116 **Table 1: Raman lidar WALI and LAASURS main characteristics. In the third column the corresponding characteristics**
 117 **of the spaceborne CALIOP lidar are also presented.**

	WALI	LAASURS
Carrier	Ground-based (truck)	Airborne
Laser	Nd:YAG, flash-pumped, Q-switched Q-smart QUANTEL	Nd:YAG, flash-pumped, Q-switched Ultra QUANTEL
Pulse length	<10 ns	6 ns
Emitted energy	120 mJ at 355 nm	30 mJ at 355 nm
Frequency	20 Hz	
Reception channels	// 355 nm ⊥ 355 nm N ₂ -Raman 387 nm H ₂ O-Raman 407 nm	// 355 nm ⊥ 355 nm N ₂ -Raman 387 nm
Reception diameter	15 cm	
Field-of-view	~2.3 mrad	
Full overlap	~200 m	
Filter bandwidth	0.2 nm	
Detector	Photomultiplier tubes	
Post processing vertical resolution	15-30 m	

118 **2.2 Airborne measurements**

119 In order to sample the low troposphere around the ground-based lidar, the ULA/Tanarg-embedded Raman lidar
 120 system LAASURS was used (Chazette and Totems, 2017). Lidar containment enabled operation for temperatures



121 down to $\sim -17^\circ\text{C}$, but with a loss of nearly 40% of the emitted energy. This has greatly limited the altitude
 122 explorations above 1 km above the mean sea level (AMSL) and we have essentially worked just above the PBL.
 123 The lidar and the ULA's flights close to the Melkoya platform are represented in Figure 4.
 124 The aircraft, Tanarg 912 XS, was built by the Air Création Company (<http://www.aircreation.fr/>) and offers a
 125 maximum total payload of $\sim 250\text{ kg}$ (Table 2). Flight durations were between 1 and 2 hours, depending on flight
 126 conditions, with a cruise speed around $85\text{--}90\text{ km h}^{-1}$. The ULA is also equipped with i) a VAISALA 300
 127 meteorological probe for temperature, pressure and relative humidity, ii) a Global Positioning System (GPS) and
 128 an Attitude and Heading Reference System (AHRS), which are part of the MTi-G components by XSens. The
 129 lidar, whose characteristics are given in Table 1, is designed to fulfill eye-safety standards (EN 60825-1). The wide
 130 field-of-view (FOV) $\sim 2.3\text{ mrad}$ allows a 90% overlap of the transmission and reception paths beyond $\sim 200\text{ m}$
 131 with the desired setting for the experiment. After correction of the overlap function, the data can be used from 150
 132 m with a negligible error compared with the one due to signal noise. The acquisition was performed by averaging
 133 400 laser shots leading to a temporal sampling close to 25 s.

134 **Table 2: Tanarg 912 XS ULA main flight characteristics.**

ULA flight characteristics	
True airspeed: 17 to 40 m s^{-1} ($60\text{ to }145\text{ km h}^{-1}$)	Endurance: 3 hr (max 4 hr at 20 m s^{-1})
Ascent speed: up to 365 ft min^{-1} (110 m min^{-1})	Maximum scientific payload: 120 kg
Descent speed: 825 ft/min (250 m min^{-1})	Maximum altitude: 5.8 km

135 2.3 Strategy and flight plans

136 We performed a total of 14 flights during the field campaign. The majority of flights were performed near the
 137 airport, around the Hammerfest peninsula. Four flights were particularly interesting for aerosol layers detection
 138 (Table 3). Three flights were not successful because of technical difficulties and the other ones were performed in
 139 low-cloud conditions, with condensation at the ceiling altitude. Only one day out of 3 was not very cloudy over
 140 the period of measurements. The more exploitable flights were performed during nighttime. Note that during the
 141 field campaign, the sun did not go down under the horizon. Each flight included a slow spiral ascent or descent
 142 where the lidar was aiming horizontally, and once at the ceiling altitude, the lidar was rotated to aim at the nadir.
 143 Flight 4 passed very close to the Melkoya platform and permitted the sampling of one active flare. Flights 10 and
 144 11 were around the Hammerfest peninsula for 2 non-consecutive hours to check the representativeness of the site
 145 for aerosols trapped within the PBL. For flight 13, the ULA took-off from Hammerfest airport at 21:38 UTC
 146 (universal time count) and headed towards North-Cape at the ceiling altitude of $\sim 1.8\text{ km AMSL}$. Before reaching
 147 North-Cape, the ULA changed heading and flew parallel to the coastline before veering towards the airport, where
 148 it landed at 23:58 UTC.

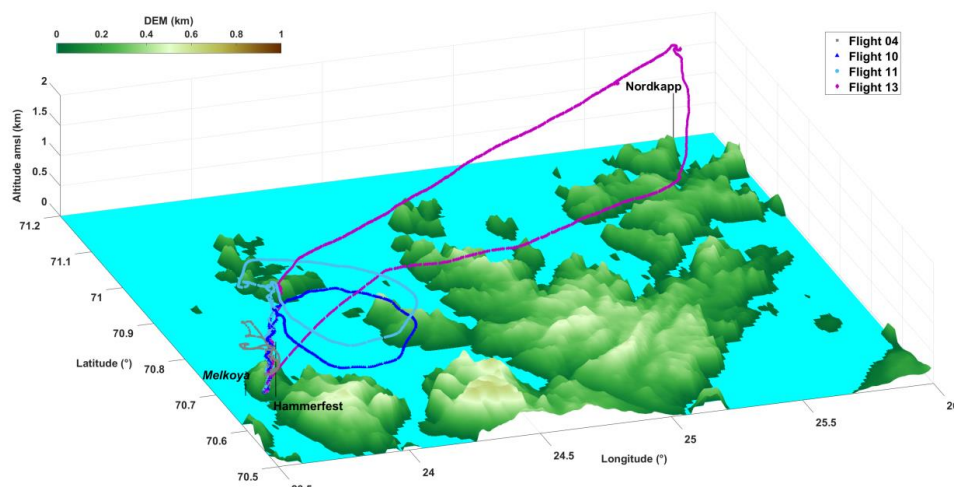
149 **Table 3: Flights information: identification, date and description.**

Flight identification	Date & hour (UTC)	Description
4	16 May, 22:39-23:24	Flight along the west coast of the Hammerfest peninsula overflying the Melkoya platform in cloudy condition.



10	20 May, 18:56-20:00	Flight around the Hammerfest peninsula in cloud free condition.
11	20 May, 23:02- 21 May, 00:26	Flight around the Hammerfest peninsula in cloud free condition.
13	22 May, 21:38-23:58	Flight towards North-Cap in cloud free condition.

150



151

152 **Figure 4: Flight plans used for this study: flight 04 on 16 May, flights 10 and 11 on 20-21 May, and flight 13 on 22 May**
 153 **(see Table 3). The flight plans are drawn over the 30 arc-second digital elevation model (DEM) GTOPO30**
 154 **(<https://lta.cr.usgs.gov/GTOPO30>).**

155 2.4 Data processing for lidar measurements

156 Lidar data analyses are not presented in detail hereafter, since the methods used have already been published (e.g.
 157 Chazette et al., 2015, and references therein). The aerosol extinction coefficient (AEC), the backscatter to
 158 extinction ratio (BER, inverse of the lidar ratio (LR)) and the particle depolarization ratio (PDR) are derived
 159 following Chazette et al. (2014) and references therein. The absolute uncertainties on the AEC are $\sim 0.01 \text{ km}^{-1}$ and
 160 the ones on the PDR are $\sim 1\text{-}2\%$ for $\text{AEC} > 0.03 \text{ km}^{-1}$. The absolute uncertainty on the BER (LR) is $\sim 0.004 \text{ sr}^{-1}$
 161 ($\sim 10 \text{ sr}$) for a mean BER (LR) of 0.020 sr^{-1} (50 sr). It decreases when the BER decreases.

162 The inversion of nadir lidar profiles acquired from the ULA is more difficult due to the noise level. For this reason,
 163 we have limited altitude excursions between 1 and 2 km AMSL. The horizontal measurements of the elastic
 164 channel are inverted to retrieve the AEC within an absolute uncertainty of 0.01 km^{-1} following Chazette and
 165 Totems (2017) and references therein. We consider a distance from the ULA between ~ 0.3 and 1.5 km after
 166 correction of the overlap function for the calculations. The nadir measurements are inverted using the constraint
 167 brought by the horizontal laser shots and the BER derived from the ground-based lidar. We therefore assume that



168 the aerosol typing does not change during the flight. Note that the N₂-Raman channel of the airborne lidar is too
169 noisy to be relevant, mainly due to the loss of emitted energy in low ambient temperature.

170 3 Large-scale data

171 3.1 Spaceborne observations

172 Active and passive spaceborne measurements were used to follow the aerosol plume transport. The horizontal
173 dispersion of the aerosol plume and its progression along the transport are highlighted with Moderate Resolution
174 Imaging Spectroradiometer (MODIS, (King et al., 1992; Salmonson et al., 1989)) onboard the polar-orbiting
175 platforms Terra and Aqua. We used a combination of the aerosol optical thickness (AOT) at 550 nm derived from
176 the two satellites. The level 2 products are provided with a spatial horizontal resolution of 10×10 km²
177 (<http://modis.gsfc.nasa.gov>). The uncertainty on the AOT is $\pm 0.15 \pm 0.05$ AOT over land and $\pm 0.05 \pm 0.03$ AOT over
178 ocean (Chu et al., 2002). The vertical structures of the aerosol layers over their sources are derived from Cloud-
179 Aerosol Lidar with Orthogonal Polarization (CALIOP) aboard Cloud-Aerosol Lidar and Infrared Pathfinder
180 Satellite Observations (CALIPSO, <http://www-calipso.larc.nasa.gov>, (Winker et al., 2007)). We have used the
181 4.10 version of CALIOP level-2 data. We mainly took into consideration the aerosol typing of (Burton et al.,
182 2015).

183 3.2 Modeling strategy

184 3.2.1 Weather model

185 The 3.5.1 version of the regional non-hydrostatic Weather Research and Forecasting (WRF) model (Skamarock et
186 al., 2008) has been used for weather simulations along the field campaign. The model was run from 7 May, to 28
187 May, 2016, with a dynamical time step of 3 min on a polar stereographic grid almost encompassing the Northern
188 Hemisphere (> 7°N). The domain has 300×300 grid points with a horizontal resolution of 50 km and 50 vertical
189 levels up to 50 hPa, considered as the top-of-atmosphere pressure. The initial and boundary meteorological
190 conditions for this hemispheric domain are provided by the 6-hourly operational analyses of the ECMWF/IFS
191 NWP model (Dee et al., 2011) from the European Centre for Medium-range Weather Forecasts (ECMWF), with
192 the support of the ESPRI (Ensemble de Services Pour la Recherche à l'IPSL, <https://www.ipsl.fr/Organisation/Les-structures-federatives/ESPRI>) team. Nudging has been applied above the planetary boundary layer (PBL) to wind,
193 temperature and humidity fields, with an update time of 6 hours. The parameterizations used are described in (Raut
194 et al., 2017) and (Marelle et al., 2017). Briefly, the prognostic turbulent kinetic energy scheme of Mellor-Yamada-
195 Janjic (MYJ) is used for the boundary layer, with the associated Janjic Eta surface layer module (Janjić, 1994).
196 Land surface processes are resolved using the Noah LSM (unified Noah land surface model (Chen and Dudhia,
197 2001)). We have used the Morrison 2-moment scheme (Morrison et al., 2009) to calculate cloud microphysical
198 properties and grid-scale precipitation. Subgrid clouds are represented using the Kain-Fritsch with Cumulus
199 Potential parameterization developed by (Berg et al., 2013). The shortwave and longwave radiation calculations
200 are performed using the RRTMG scheme (Rapid Radiative Transfer Model for Global applications; (Iacono et al.,
201 2008)).
202



203 3.2.2 *Back-trajectories*

204 The Lagrangian particle dispersion model FLEXPART-WRF (Brioude et al., 2013) derived from the FLEXPART
205 model (Stohl et al., 2005) is run in this study to investigate the origin and transport pathways of air masses bringing
206 aerosols to Hammerfest. Three backward simulations are performed on 15 May, 05:00 UTC, 20 May, 20:00 UTC
207 and 22 May, 21:00 UTC to provide insight into the representation of aerosol transport to Scandinavia. In each of
208 them, a total of 10 000 particles are released at Hammerfest in a volume of 50 km x 50 km large and 1 km (200 m)
209 thick for 15, 20 May (22 May) centered on the aerosol plumes detected aloft. The origin of each air parcels is then
210 established using the meteorological fields simulated by WRF (Sect. 3.2.1). As transport durations are typically
211 less than 9 days, this approach finally allows us to track the air mass origin over the source regions of interest. As
212 a proxy to represent the source-receptor relationships, we use the PES (potential emission sensitivities) that
213 quantify the amount of time spent by the particles in every grid cell.

214 4 Aerosol observed in the Arctic troposphere

215 There are few clear sky periods during the campaign, as is often the case over the studied area. The interesting
216 periods are given in terms of AEC and PDR in Figures 5 to 7 (14-15, 20-21, and 22-23 May, 2016), where
217 outstanding high-altitude features are highlighted. The temporal evolutions of the AEC profile are given in local
218 time (LT) corresponding to UTC+2.

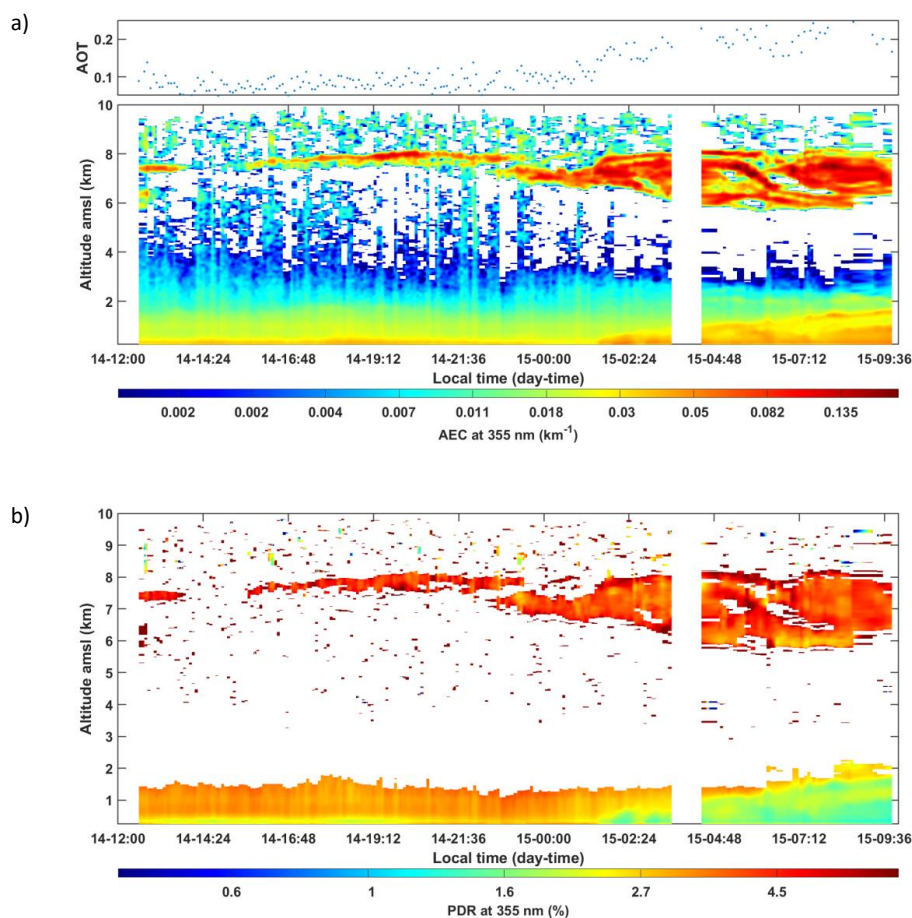
219 4.1 Optical properties of aerosol layers derived from the ground-based lidar

220 The coupling between the elastic and the N₂-Raman channels is used to derive the BER for the different aerosol
221 layers. The molecular contribution is corrected using the hourly vertical profiles of temperature derived from WRF
222 and a classical modeling of the Rayleigh scattering (Bodhaine et al., 1999). The troposphere has been divided into
223 two altitude ranges, as the lower and upper layers are not necessarily composed of the same aerosol types. The
224 first aerosol layer is located between the ground level and ~2.5-3 km AMSL and the second one above 3 km
225 AMSL. The retrieval of the BER for each layer and each measurement period is given in Figure 8. The correct
226 estimate of the BER is obtained when the optical thickness derived from the elastic channel of the lidar is very
227 close to that deduced from the N₂-Raman channel (Chazette et al., 2017).

228 On 14-15 May, the mean BER is ~0.018 sr⁻¹ for the upper layer with a standard deviation of 0.002 sr⁻¹ (now noted
229 ~0.018±0.002 sr⁻¹), whereas as BER is ~0.028±0.003 sr⁻¹ in the lower troposphere (Figure 8a). Due to the
230 uncertainty linked to the overlap function, the sensitivity of the first 200 m where marine aerosols may
231 significantly contribute is lesser. Nevertheless, the higher value observed in the vicinity of the PBL is likely to be
232 associated with a contribution of marine aerosols (BER~0.04 sr⁻¹ (Flamant et al., 1998a)). The bottom layer
233 depolarizes very slightly the lidar signal, with PDR <3% and even highlights a lower signature (~1.5%) after 0230
234 LT. It may be due to a larger oceanic contribution, which leads to an increase of the AEC in the PBL (~0.04 km⁻¹).
235 The upper layer has slightly higher PDR values, of the order of 5-6%. Within this range of PDR, the particles
236 cannot be dust-like aerosols. Nonetheless, they are likely to be pollution or biomass burning particles transported
237 toward the measurement site. The total AOT, without the upper layer, is close to 0.08 at 355 nm and increase up
238 to ~0.2 in presence of the higher aerosol plume (Figure 5).

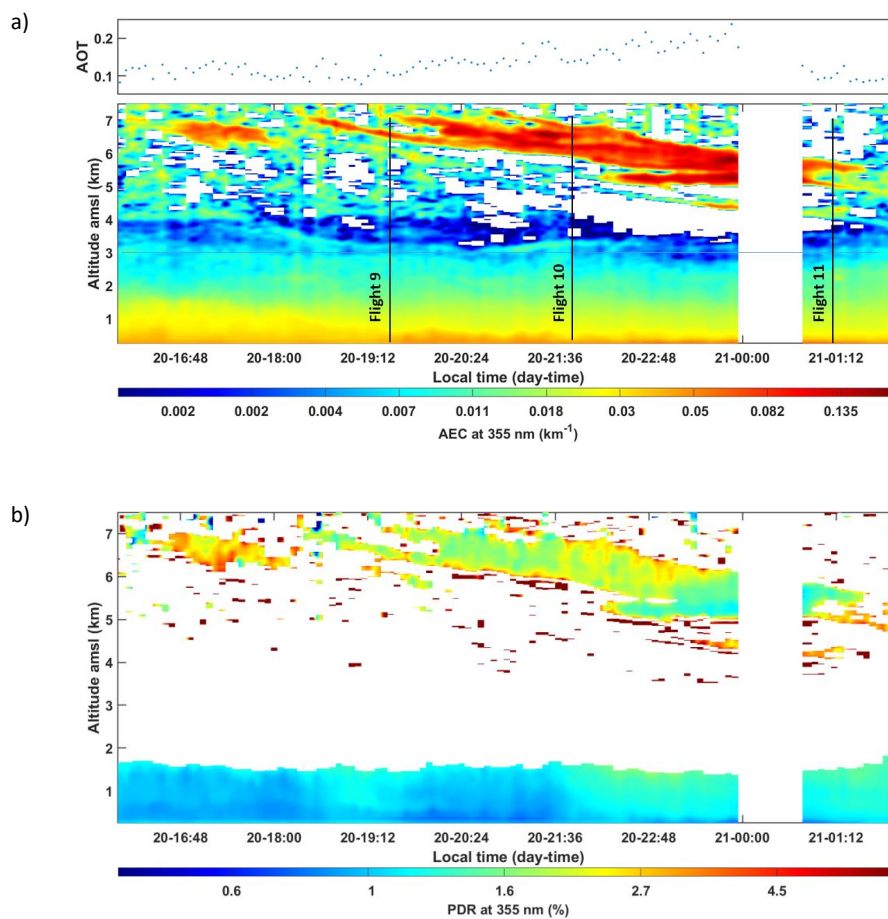


239 The BER is smaller ($0.012 \pm 0.002 \text{ sr}^{-1}$, Figure 8b) for the upper layer on 20-21 May, a typical value expected for
240 pollution and/or biomass burning aerosols. The PDR is also smaller with a mean value close to 1.5%. The aerosols
241 in the lower troposphere exhibit a larger BER ($0.037 \pm 0.003 \text{ sr}^{-1}$), demonstrating a strong influence of the oceanic
242 sources. There are also associated with a small PDR, $\sim 1\%$. The AOT in the lower atmosphere is similar to the one
243 on 14-15 May. The elevated aerosol plume presents an excess AOT close to 0.1 at its maximum (Figure 6).
244 The third period of interest (22-23 May) shows a tiny plume in the middle troposphere, between 3 and 4 km AMSL
245 (Figure 7), with a very small AOT excess (~ 0.03). The BER (Figure 8c) and PDR are similar to the ones of 20-21
246 May, $0.013 \pm 0.002 \text{ sr}^{-1}$ and $\sim 2\%$, respectively. The layer underneath is less influenced by marine aerosol and shows
247 a BER close to $0.014 \pm 0.003 \text{ sr}^{-1}$, more characteristic of polluted particles. Nonetheless, the layer under 400 m
248 AMSL is more difficult to sample by the lidar and may contain a significant contribution of marine aerosols, as
249 suggested by the slight decrease in PDR (Figure 7b).



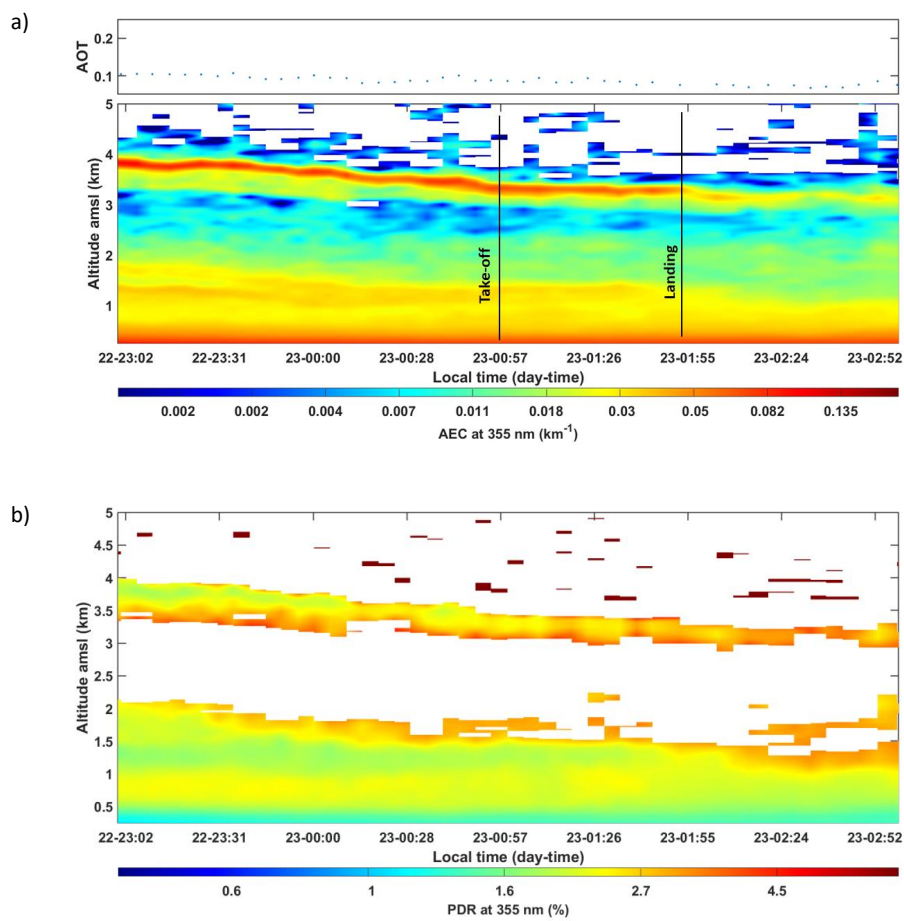
250 **Figure 5: Temporal evolutions of a) the lidar-derived aerosol extinction coefficient (AEC) and the aerosol optical**
251 **thickness (AOT); b) the particle depolarization ratio (PDR), at the wavelength of 355 nm, from 14 to 15 May, 2016.**

252



253 Figure 6: As Figure 5 but from 20 to 21 May, 2016.

254

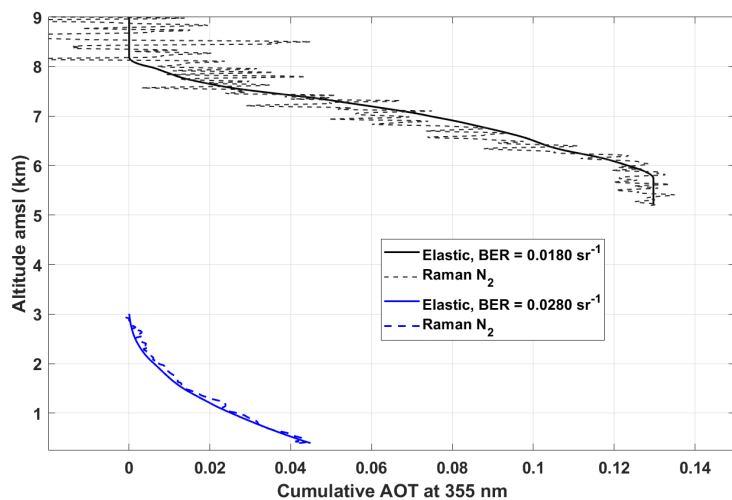


255 Figure 7: As Figure 5 but between 22 and 23 May 2016.

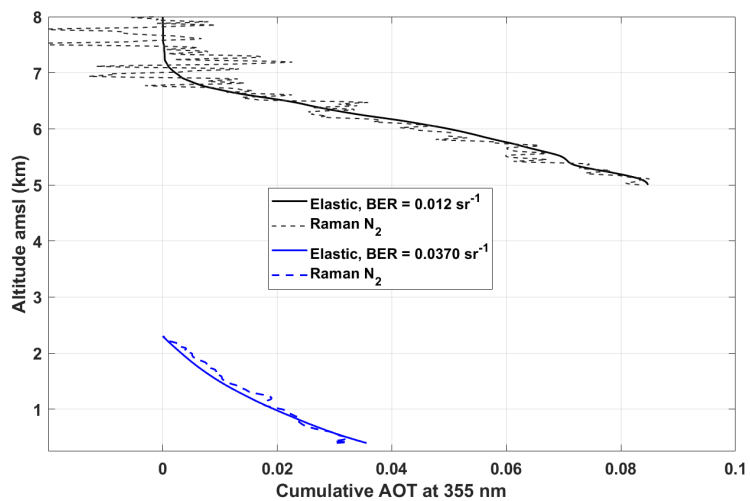
256

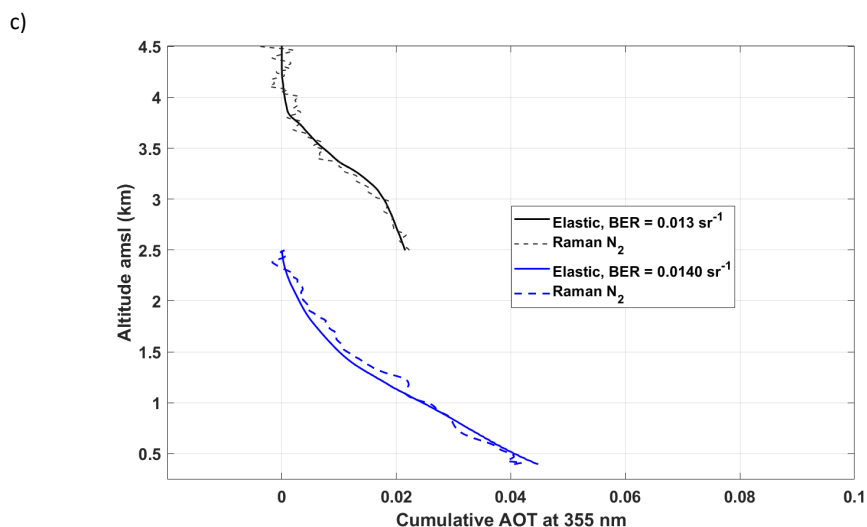


a)



b)





257 **Figure 8: Cumulative aerosol optical thickness (AOT) derived from both the N₂-Raman (dashed line) and the elastic**
258 **(continuous lines) channels for the upper (black lines) and the lower (blue line) aerosol layers at 355 nm: a) 14-15 May;**
259 **b) 20-21 May; c) 22-23 May.**

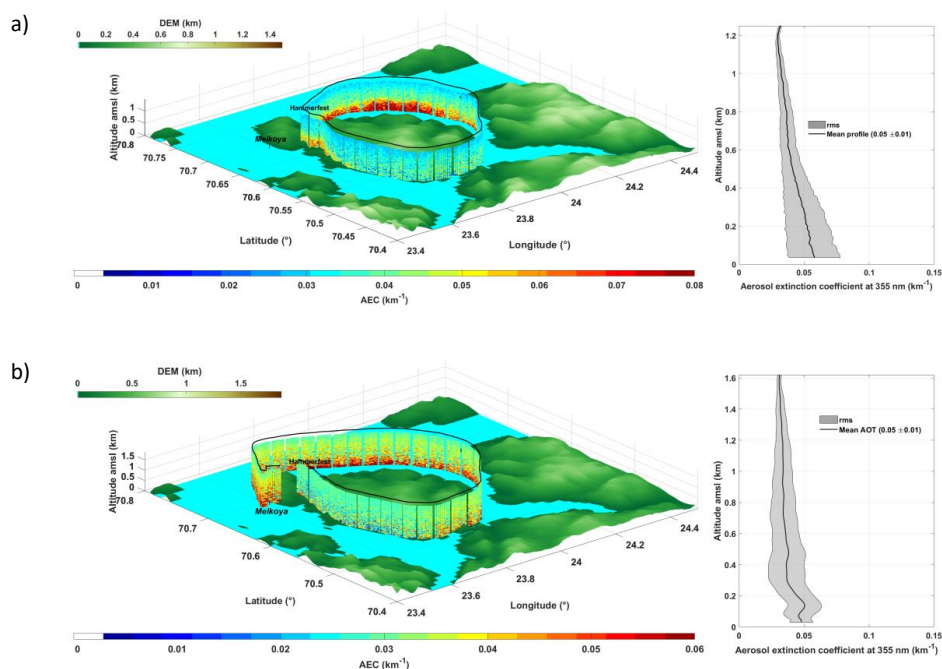
260 4.2 Homogeneity of aerosol layers within the lower troposphere

261 The lidar-derived aerosol optical properties in the lower troposphere look like homogeneous structures that can be
262 related to the specific situation of the ground-based site. Different sources of aerosols may influence the PBL, the
263 main ones being marine aerosols and anthropogenic aerosols generated in the Hammerfest region (domestic
264 combustion, industrial activity, shipping emissions). To verify the representativeness of the local measurements,
265 we used lidar measurements from the ULA.

266 4.2.1 Marine contribution

267 The AEC retrieved for flights 10 and 11 are given in Figure 9 with the mean vertical profiles between the ground
268 level and the ceiling flight altitude in both cases, AOTs are low with a small variability of the order of 0.05 ± 0.01 .
269 Higher AECs are observed in the northeastern part of the flights (red areas). Because we did not detect many ships
270 in this area, those AEC enhancements are probably due to sea-salts. They may be transported over the nearby coast
271 as the result of the interactions between wind surface and sea (Blanchard and Woodcock, 1980; Flamant et al.,
272 1998b). We note that local pollution is missing altogether.

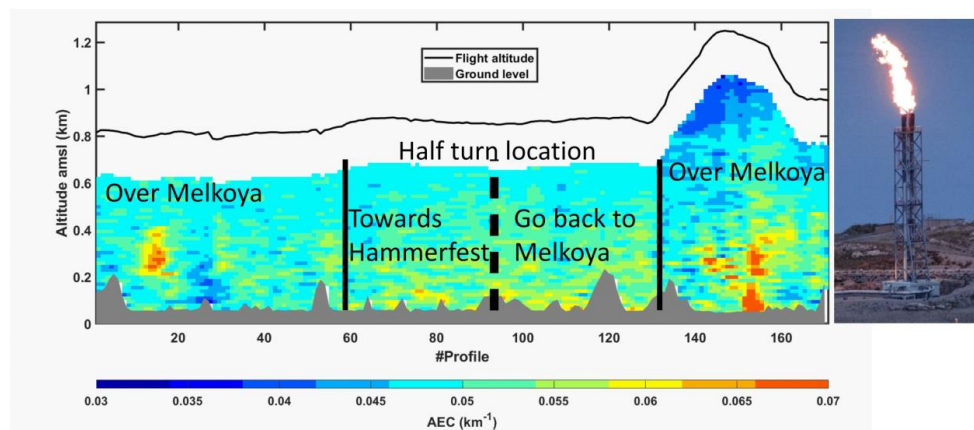
273



274 **Figure 9: Vertical profiles of the aerosol extinction coefficient (AEC) derived from the lidar onboard the ULA: a) flight**
275 **10 and b) flight 11. The mean AEC vertical profiles and their dispersions are given on the right table. As in Figure 4,**
276 **the flights are plotted over the digital elevation model (DEM) GTOPO30.**

277 4.2.2 Gas flaring contribution

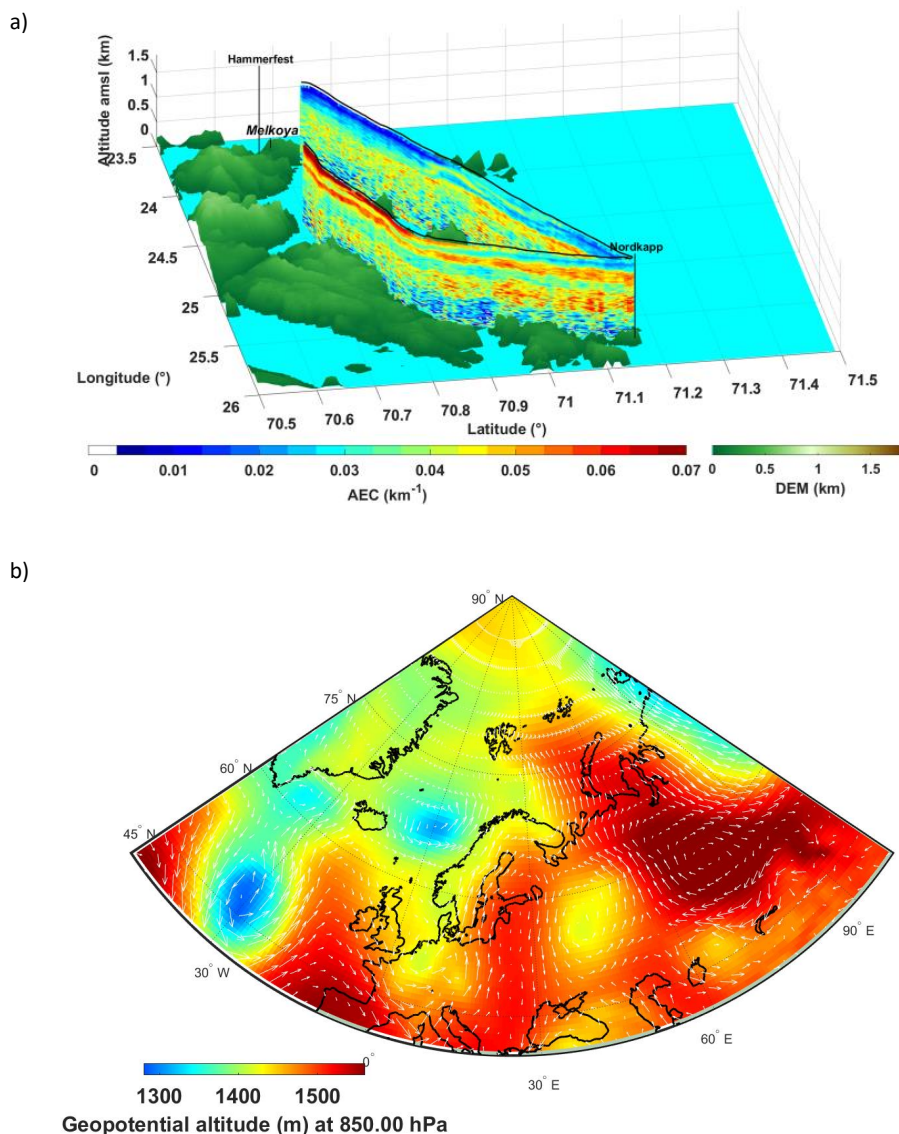
278 The proximity of the gas rig from the Melkoya facility suggests the presence of an industrial source of aerosol and
279 needed to be quantified. The lowest chimney (~ 46 m, $70^{\circ}41'20''$ N $23^{\circ}35'59''$ E) of the Melkoya site used for the
280 low-pressure flare was regularly active during the field experiment and more especially on 16 May (flight 4). The
281 flare (Figure 10, right picture) at the time of sampling was ~ 20 m above the chimney, with a width ~ 5 m. On that
282 day, flare smoke presented some blackish color because some hard hydrocarbons (condensate) were present in
283 flare gas. The flight pattern shown in Figure 4 is elongated in Figure 10 using profile number for the sake of clarity.
284 The locations of the ULA when it was close to the flare are highlighted (profiles $\sim \#18$ and $\sim \#154$) and correspond
285 to the higher AEC of ~ 0.07 km^{-1} . For the second pass, the flare plume is detected from its emission source. The
286 contribution of this flare emission to the AOT is low, ~ 0.02 at 355 nm for a total AOT between the ground level
287 and 1 km AMSL of ~ 0.04 . The calculation has been done with a BER ~ 0.037 sr^{-1} and may be underestimated by
288 a factor of 2, as experimental means for a better constraint do not exist. Nevertheless, we note that taken
289 individually, it is a small contribution to the local pollution (representing half of the aerosol background in the first
290 kilometer) and it is very localized in space.



291
292 **Figure 10:** Left table: Vertical profile of the aerosol extinction coefficient (AEC) during the flight 4 (16 May, 2239-2324
293 local time) dedicated to the sampling of the Melkoya flare at 355 nm. Right picture: Flare sampled by the airborne lidar
294 over the Melkoya platform.

295 4.2.3 Northern contribution

296 During the duration of the experiment, we did not observe any specific contribution to the aerosol load in the
297 lowest troposphere above the PBL. An exception was for Flight 13 on 22 May, 21:38-23:58 UTC, which was the
298 longest flight we performed. The vertical profiles of the derived AEC following this flight are plotted on Figure
299 11a. In the first part of the flight, we note an increase in the AEC close to the ceiling altitude of ~1.7 km AMSL
300 with values over 0.07 km^{-1} . Similar values are measured throughout the flight above the PBL (in red in Figure
301 11a). The AOT is ~0.06 above the continent and decreases above the ocean (~0.04). The means of constraint are
302 also limited in this case, because the signal-to-noise ratio for the N_2 -Raman channel was not high enough and a
303 BER of 0.014 sr^{-1} , initially derived from the ground-based lidar, has been used. The measurements performed
304 during the flight whilst aiming horizontally are also used as constraints. The aerosol layer has been identified as
305 coming from the Murmansk region, Russia. The air mass moves along the coast from east to west, drawn by a low
306 off the Norway coast along the Greenwich meridian. This low is clearly visible in the Figure 11b and is responsible
307 for the air mass curvature before its northward motion towards Hammerfest and the North Cape.



308 Figure 11: a) Vertical profiles of the aerosol extinction coefficient (AEC) derived from the lidar onboard the ULA for
309 flight 13 on 22 May, 21:38-23:58 UTC. As in Figure 4, the flights are plotted over the digital elevation model (DEM)
310 GTOPO30. b) Geopotential altitude for the pressure level of 850 hPa (~1.6 km AMSL). The wind field at 850 hPa is also
311 indicated in white arrows.

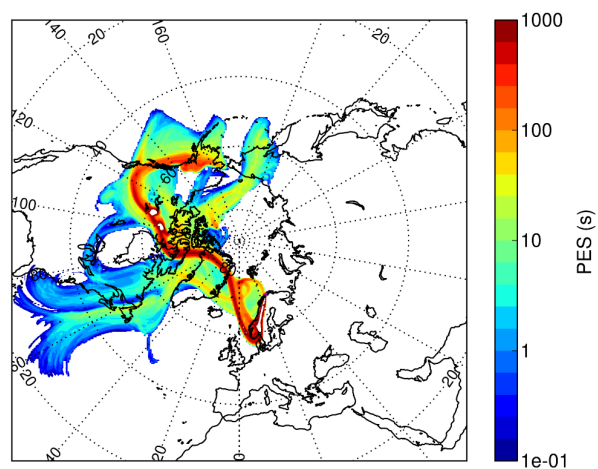
312 5 Origin of the upper tropospheric aerosol plumes

313 To investigate the origin of the three upper aerosol layers, 9-days back trajectories have been performed using
314 FLEXPART-WRF and constrained by the meteorological fields simulated by WRF over the Arctic region. The

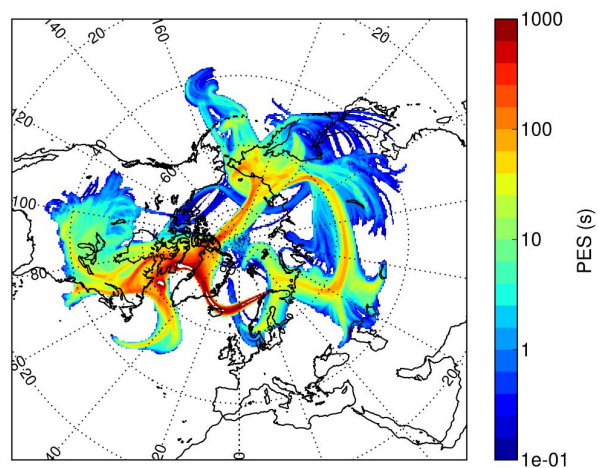


315 results are given in terms of PES in Figure 12. These simulations are compared, where possible, with the MODIS
316 and CALIOP space observations to confirm the result.

a)

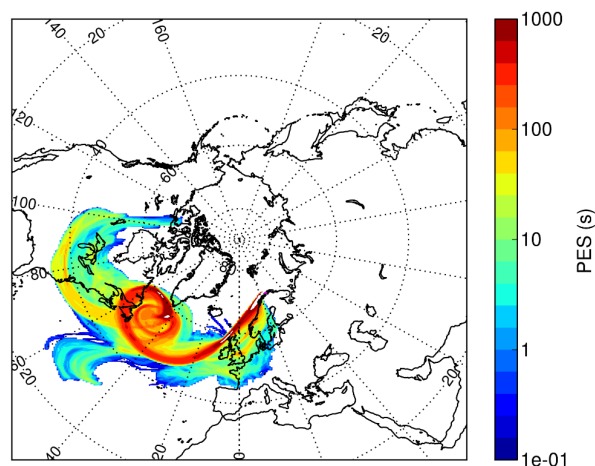


b)





c)

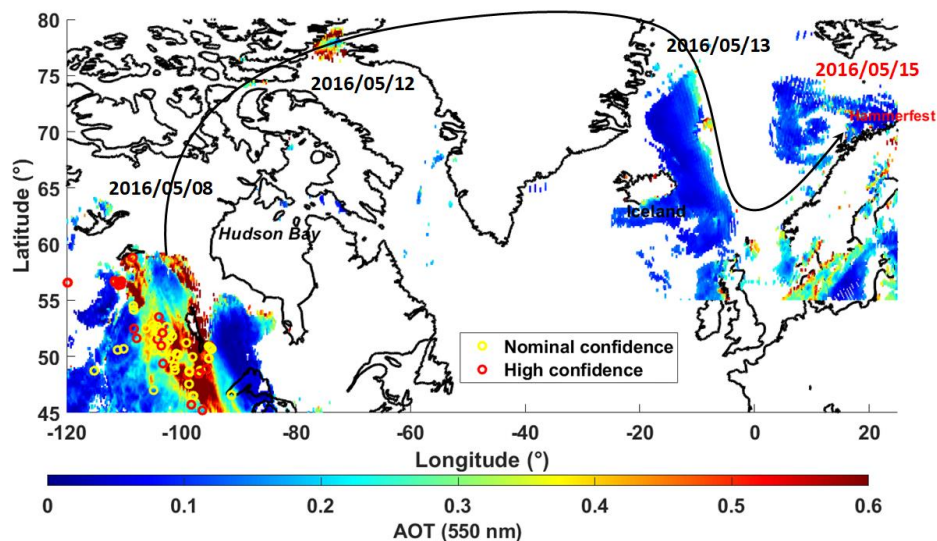


317 **Figure 12: 9-days back trajectories for the upper aerosol plume observed over Hammerfest on: a) 14-15 May, b) 20-21**
318 **May and c) 22-23 May, 2016. The back trajectories are given in terms of potential emission sensitivity (PES).**

319 **5.1 Aerosol plume on 14-15 May**

320 On May, 8-9, an aerosol plume was injected in the higher troposphere following the strong forest fires which
321 occurred close to Fort McMurray (56.72°N 111.38°W, North-Eastern Alberta, Canada). As shown in Figure 13,
322 the aerosol plume has been sampled by MODIS on 8 May, with an AOT larger than 0.4 at 550 nm. In the same
323 figure, the thermal anomalies derived from MODIS are also given for both the nominal and the high confidence
324 levels. The aerosol typing derived from CALIOP is plotted in Figure 14a. It confirms the injection of biomass
325 burning aerosols between 6 and 7 km AMSL. The plume then moves north-west of Hudson Bay and reaches Baffin
326 Sea on 12 May. It then crosses Northern Greenland and goes on to cross the Greenland Sea on 13 May. A
327 pronounced northerly flow finally brings the plume to Hammerfest, bypassing the low pressure system located off
328 Norway and responsible for the plume curvature. Elevated smoke aerosols are identified by CALIOP over the
329 Baffin Sea and Greenland Sea as shown in Figure 14b and Figure 14c, respectively.

330 We observed a similar transport of biomass burning aerosol over the Mediterranean Sea, leading to a BER of 0.025
331 sr^{-1} (Chazette et al., 2016) higher than the one retrieved here ($\sim 0.018 \pm 0.002 \text{ sr}^{-1}$). There is no reason for a typical
332 BER value for biomass burning aerosols. Indeed, the BER is highly dependent on the chemical composition of
333 aerosols via the complex refractive index, but also on their size distribution. Furthermore, both size distribution
334 and chemical composition of biomass burning aerosols depend on the type of combustion and the intensity of the
335 fire. Moreover, aerosols age during transport. Hence, a wide range of BER values is likely for biomass burning
336 aerosol after a long-range transport (Amiridis et al., 2009).

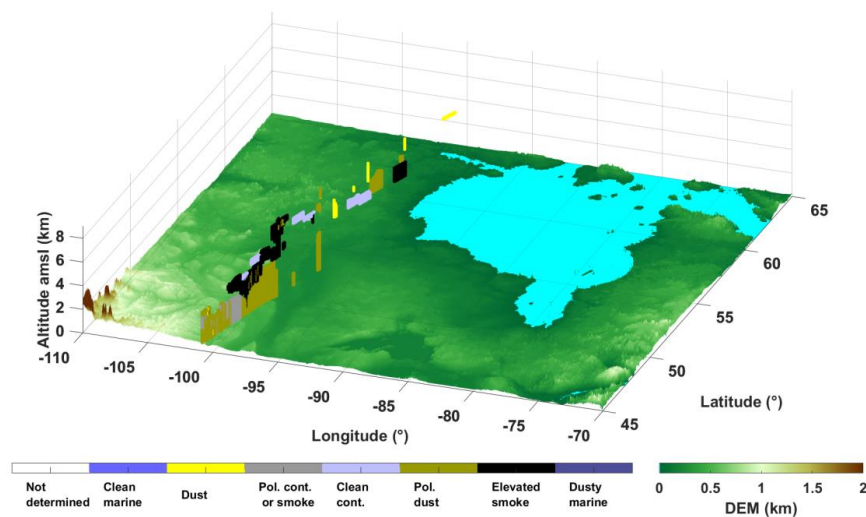


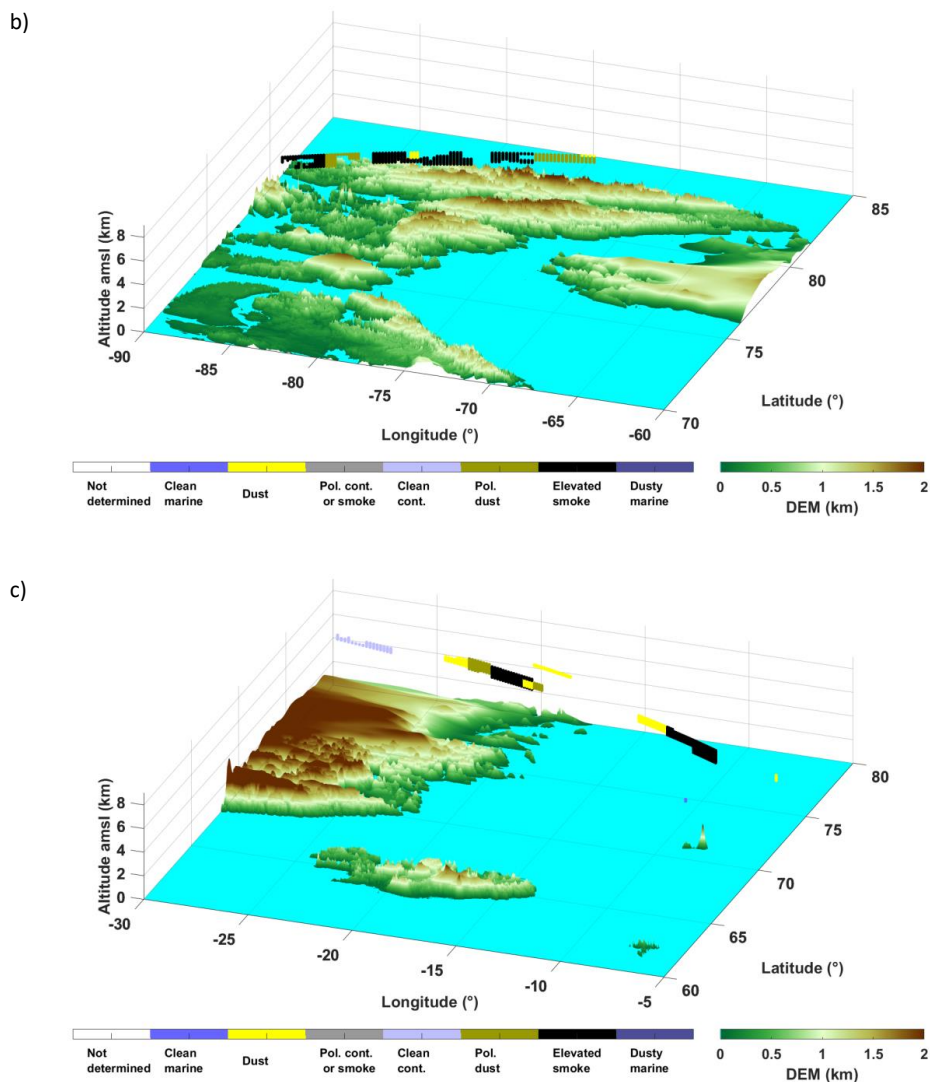
337

338 **Figure 13: MODIS-derived aerosol optical thickness (AOT) at 550 nm for three different days and locations. The dates**
 339 **are indicated in the figure. The thermal anomalies derived from the MODIS fire product are also given on 8 May, 2016,**
 340 **corresponding to the origin of the studied aerosol plume studied. The route followed by the biomass burning plume is**
 341 **represented by a black solid line. It begins on 8 May, to finish on 15 May.**

342

a)





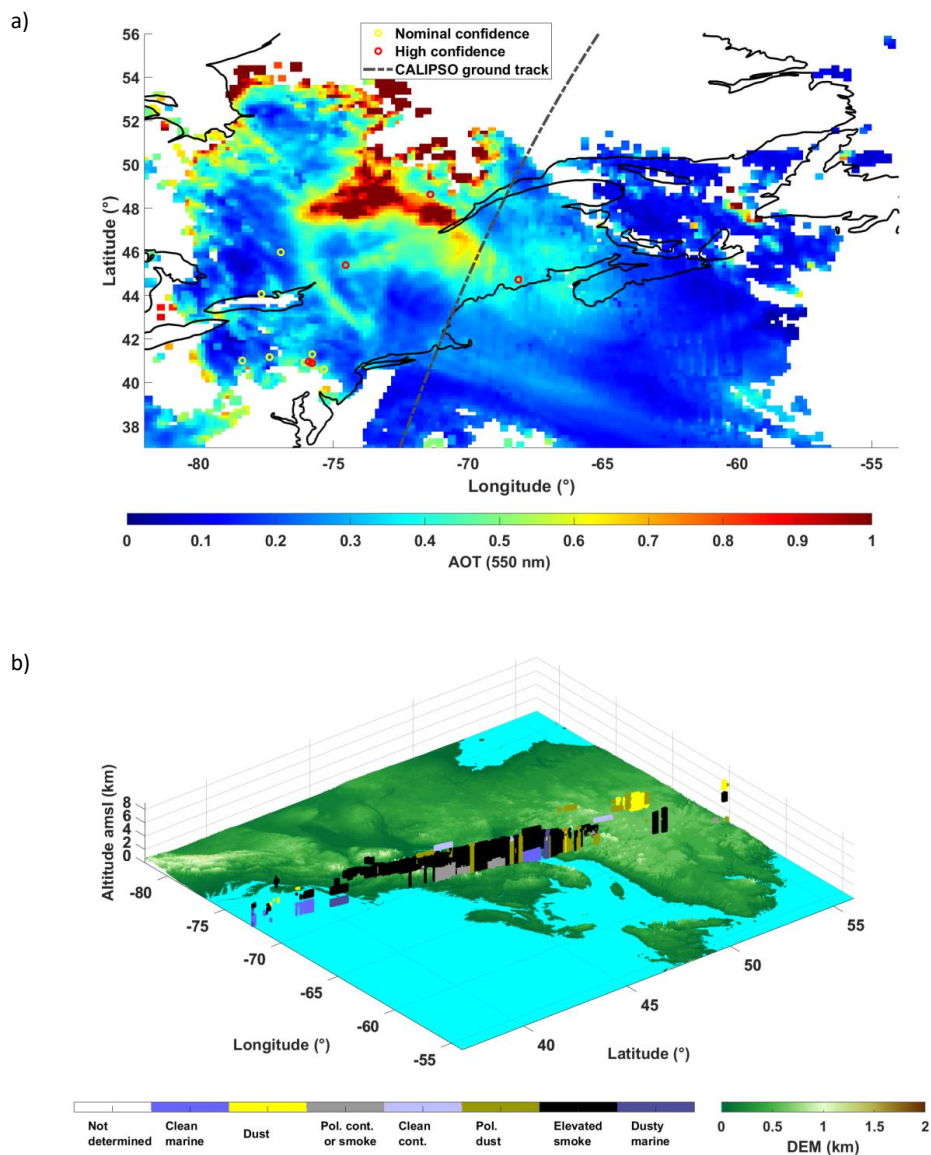
343 **Figure 14: CALIOP-derived aerosol typing for a) the Fort McMurray on 8 May, b) the Baffin Sea on 12 May, and c)**
344 **the Greenland Sea on 13 May, corresponding to the plume identified by MODIS in Figure 13.**

345 5.2 Aerosol plume on 20-21 May

346 As for the previous aerosol plume, the origin seems to be from Canada. The back trajectories show potential
347 contributions from Russia, but checking the spaceborne observations corresponding with the potential plume
348 location, we do not identify any forest fires or anthropogenic emissions. The Canadian origin could not be clearly
349 established from MODIS observation due to strong cloud cover. A large plume ($AOT > 0.8$) is found over the
350 St. Lawrence region on 12 May, (Figure 15a) and corresponds to the transport of air masses along the back
351 trajectories. Continuing the back trajectories, the Fort McMurray area, where forest fires have persisted, also
352 appears to be the main source. An orbit of CALIPSO passes over the eastern part of the plume on 12 May, and



353 shows that it is mainly composed of elevated smoke aerosols from Canada (Figure 15b). The BER that has been
354 found (0.012 sr^{-1}) can also be attributed to biomass burning aerosols. However, given the possible values, it is not
355 a criterion.



356

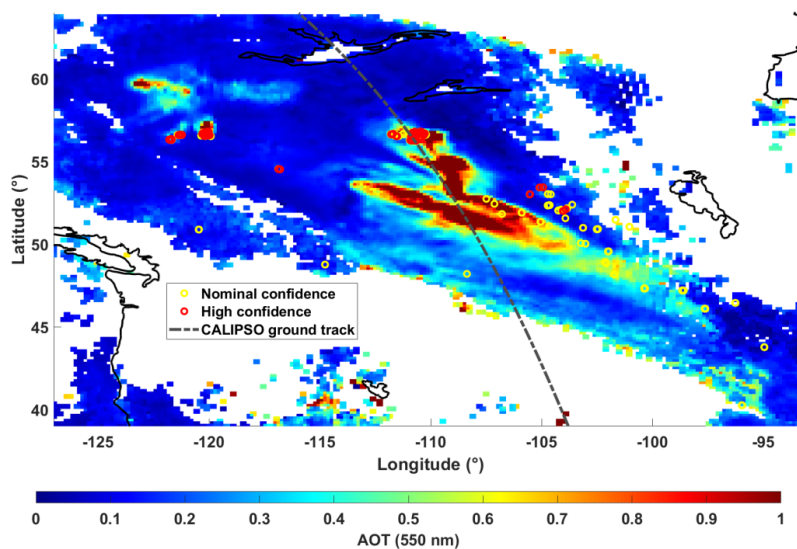
357 Figure 15: a) MODIS-derived aerosol optical thickness (AOT) at 550 nm and thermal anomalies on 8 May, 2016; b)
358 CALIOP-derived aerosol typing (orbit 2016-05-12T06-53-10Z). The CALIPSO ground track is indicated in a).

359 5.3 Aerosol plume on 22-23 May

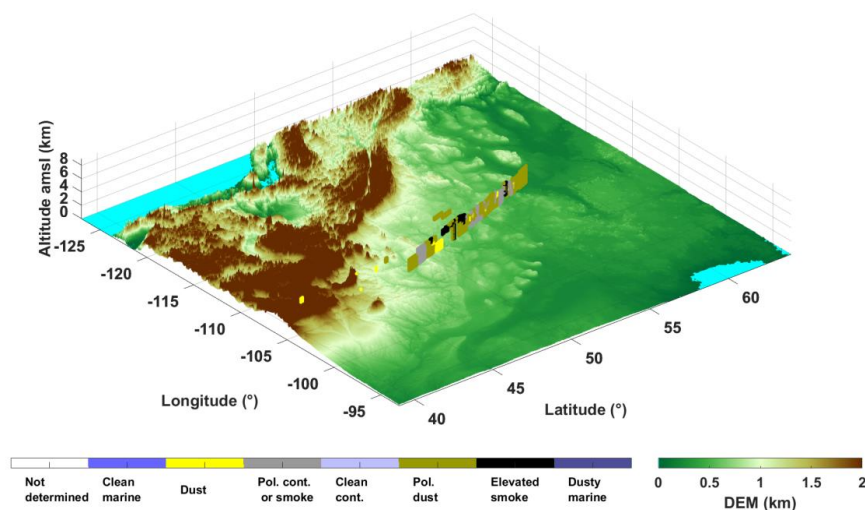


360 The origin of this last aerosol plume is more easily identified to be the Canada, also in the area of Fort Mc Murray,
361 on 15 May. The aerosol plume emitted by the forest fires is well circumscribed by MODIS with AOTs greater
362 than 1. The locations of the fires are also indicated by the thermal anomaly. The CALIPSO orbit passes just above
363 the plume and offers the possibility to characterize the aerosols as elevated smoke, polluted continental or smoke
364 and polluted dust. As for the aerosol plume on 20-21 May, the same remark can be made on the derived BER of
365 0.013 sr^{-1} .

a)



b)



366



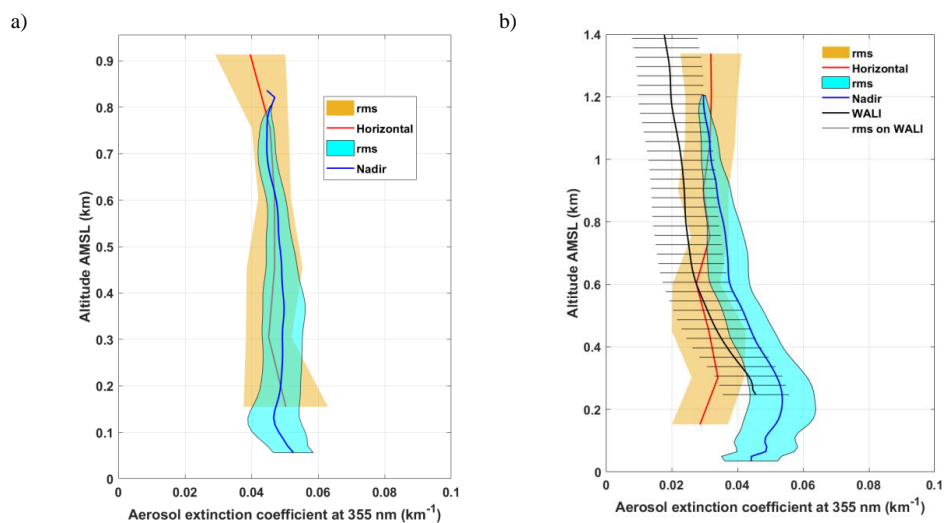
367 **Figure 16:** a) MODIS-derived aerosol optical thickness (AOT) at 550 nm and thermal anomalies on 15 May, 2016; b)
368 CALIOP-derived aerosol typing (orbit 2016-05-15T19-42-56ZD). The CALIPSO ground track is indicated in a).

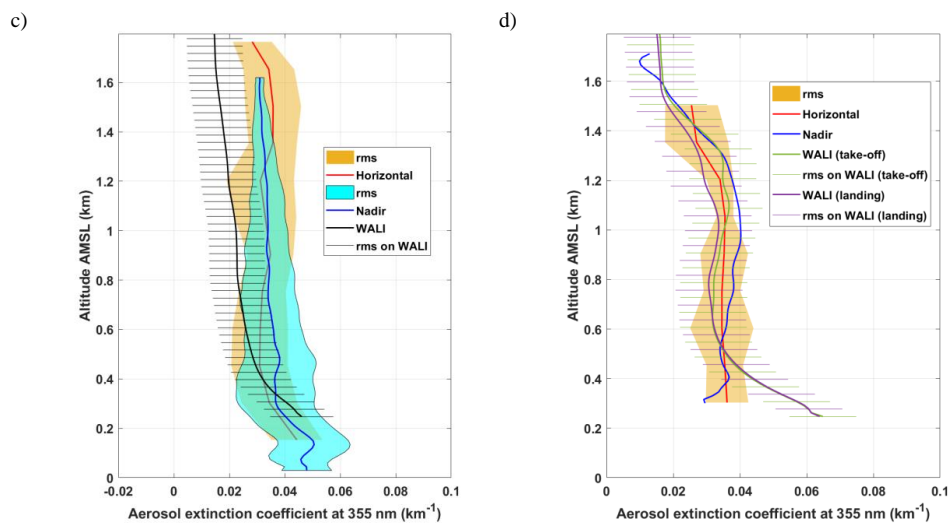
369 **6 Data coherence**

370 **6.1 Coherence on the vertical profiles**

371 For higher altitude aerosol layers, we do not have any airborne observations to check the consistency of the results
372 with the lidar embedded on the ULA. Nonetheless, we have that possibility for the lower troposphere. Figure 17
373 shows the comparison between different approaches to retrieve the AEC vertical profile within the first 2 km of
374 the atmosphere. Horizontal and nadir lines of sight measurements performed from the ULA are compared for the
375 4 flights considered. We consider the closer 10 nadir profiles from the location of the spiral ascent (or descent). In
376 all the cases, the AEC profiles derived from the different approaches are all in agreement within 0.01 km^{-1} of
377 uncertainty.

378 On 16 May, ground-based lidar data are not available due to low cloud cover. For the three other days, the 20
379 profiles closer in time to the airborne lidar profiles are considered. They are plotted with a solid line, together with
380 their error bars in Figure 17b-d. For the flights 10 and 11 a slight underestimation is noted, but error bars overlap
381 (within $\sim 0.01 \text{ km}^{-1}$). The WALI-derived AEC profile is a better match with the ones derived from the airborne
382 lidar for flight 13, except in the PBL where they highlight a larger AEC. Such a discrepancy may be due to the
383 fact that measurements from the ULA were mainly performed over the ocean (Figure 11a). Note that the AEC
384 profile derived from nadir measurement is not drawn with its rms to lighten the figure, knowing that it is like that
385 of other flights.



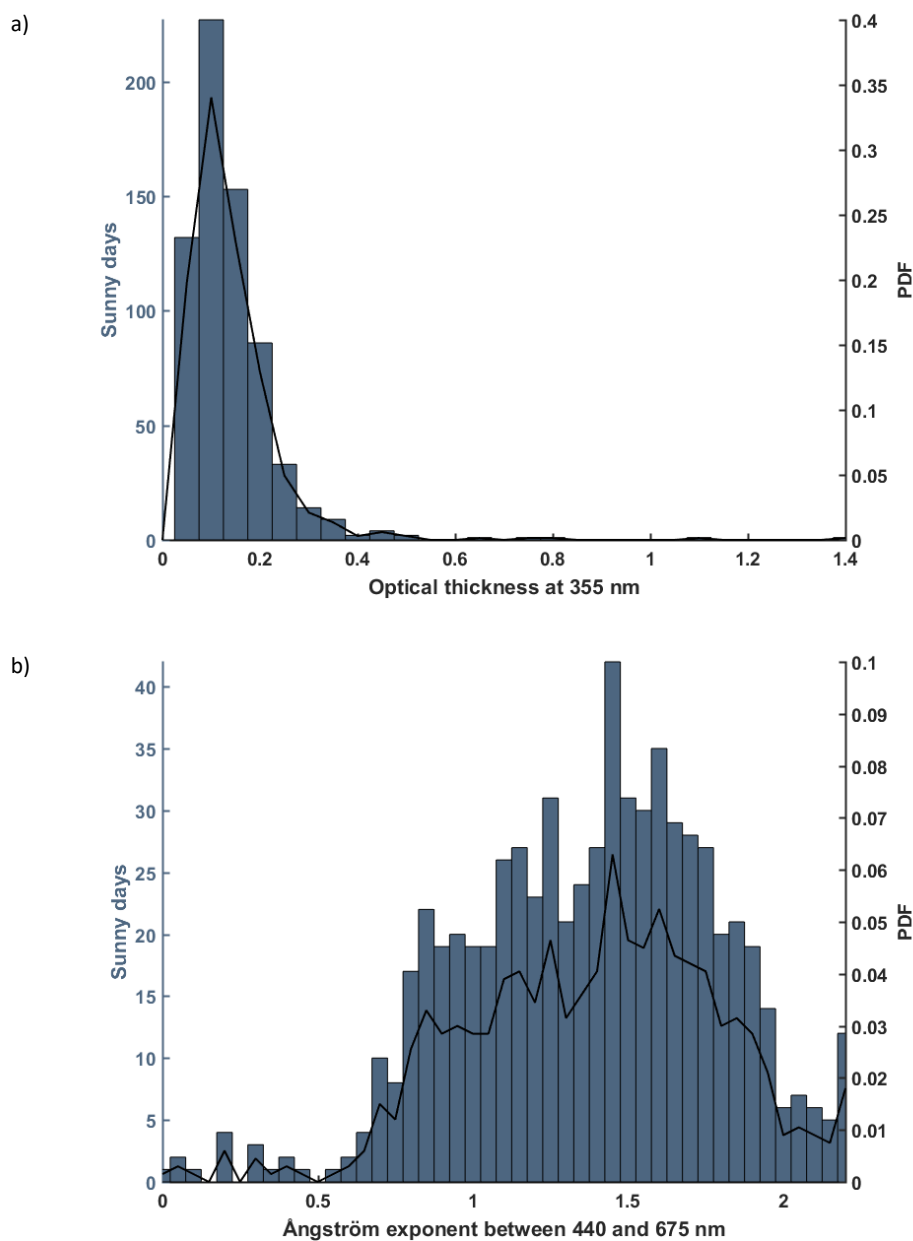


386 **Figure 17:** Vertical profiles of the AEC derived from the airborne and ground-based lidars for times corresponding to
387 a) flight 4, b) flight 10 & 11, and d) flight 13.

388 6.2 Coherence on the aerosol optical thickness

389 Lidar-derived AOTs are checked against a SOLAR Light[®] Microtops II manual sunphotometer. The measurements
390 were performed in clear sky condition during the three observation periods presented in Table 3. Measurements
391 have not been continuous, since they have been carried out alternatively with lidar observations. On 13 and 14
392 May, mean AOT at 355 nm of 0.059 ± 0.005 is derived and matches very well the value retrieved from lidar
393 measurement outside the upper aerosol plume. In the same conditions, we report AOTs of 0.084 ± 0.005 and 0.073
394 ± 0.005 on 19 and 20 May, respectively. Note that manual solar targeting induces an additional non-systematic
395 bias, which leads to an absolute uncertainty assessed as of the order of 0.03 when comparing with simultaneous
396 measurements by an automated sunphotometer before the field campaign.

397 We note a low background AOT over Hammerfest, which is between 0.06 and 0.08 at 355 nm ($\sim 0.04 \pm 0.01$ at
398 550 nm). Such a value appears to match the one derived from the available MODIS data leading to $\sim 0.05 \pm 0.06$
399 during the entire field campaign. To consider a longer time frame, we give the histograms of AOT and Ångström
400 exponent from 2008 to 2016 for the closer AERONET station of Andenes (69N 16E, ~ 320 km southwest of
401 Hammerfest) in Figure 18. The mean AOT at 355 nm is lower than 0.1 with a standard deviation of ~ 0.5 . The
402 Ångström exponent is very variable, mainly between 0.5 and 2, due to long-range transport aerosol (anthropogenic
403 pollution, biomass burning and Saharan dust) originated in central and eastern Europe (Rodríguez et al., 2012).
404 Note that the Ångström exponent derived from the manual sunphotometer is between 1.2 and 1.7, when
405 considering the wavelengths of 380 and 500 nm.



406 Figure 18: Histograms of a) the aerosol optical thickness at 355 nm and b) the Ångström exponent between 440 and 675
407 nm for the AERONET station of Andenes (69N 16E). The data are for the clear days between 2008 and 2016. The
408 probability density functions (PDF) are also given.

409 7 Conclusion



410 This work contributes to shed light on the abundance of aerosols in late spring over the European Arctic. During
411 the PARCS field-campaign, from 13 to 26 May, 2016, we collected an original dataset of remote sensing
412 measurements performed with ground-based and airborne (ULA) lidars. We evidenced 3 cases of aerosol long-
413 range transport over 2 weeks, originating from the Fort McMurray area, where strong forest fires occurred. They
414 followed different pathways to reach Northern Norway, but they significantly increased the AOT by a factor of up
415 to ~2. The AOT was enhanced from a background value of ~0.08 (~0.05), if not less, to ~0.2 (0.12) at the
416 wavelength of 355 nm (550 nm). This may imply a strong influence of long range transport of biomass burning
417 aerosols on the radiative budget over the Arctic area.

418 In the lower troposphere, below 3 km AMSL, the aerosol load is weak and corresponds to the previously observed
419 background value. In Hammerfest, airborne lidar measurements have shown a strong homogeneity of the PBL.
420 The main causes inducing a heterogeneity are i) the marine aerosol production, which is a function of the surface
421 wind speed, ii) the advection of northern air masses from industrial sites in Russia (Murmansk region), and iii) the
422 contribution of the Melkoya facility flares. We noted a very local effect of the active low-pressure flare, with an
423 enhancement close to 0.02 of the AOT at 355 nm. The effect on the environment therefore appears to be weak.
424 Because this plant is rather isolated, extending the conclusions to larger oil and gas rigs like those identified in
425 Figure 1 is hardly possible and would be purely speculative.

426 From an experimental perspective, the coupling between ground-based and airborne lidar measurements proved
427 to be essential for data analysis. The lidar systems are complementary and the coupled approach allows
428 confirmation of the results. With ULA flights, however, we remain in the vicinity of the ground station and flights
429 with larger carriers would be more suited to the regional scale. Nevertheless, one would lose in flexibility of
430 execution and in repetitiveness of measurement, inevitably limited by the cost of the flights.

431 **Acknowledgments:** This work was supported by the French Institut National de l'Univers (INSU) of the Centre
432 National de la Recherche Scientifique (CNRS) via the French Arctic initiative. The Commissariat à l'Energie
433 Atomique et aux énergies alternatives (CEA) is acknowledged for its support. We thank Yoann Chazette, Nathalie
434 Toussaint and Sébastien Blanchon for their help during the field experiment. The ULA flights were performed by
435 Franck Toussaint. The Avinor crew of Hammerfest Airport, represented by Hans-Petter Nergård, and the company
436 Air Creation company are acknowledged for their hospitality. Dr. K. S. Law is acknowledged for securing the
437 funding of the Pollution in the ARctic System campaign. Support on computer modeling by T. Onishi was granted,
438 allowing access to the HPC resources of IDRIS under the allocation A001017141 made by GENCI, and to the
439 IPSL mesoscale computing center (CICLAD: Calcul Intensif pour le Climat, l'Atmosphère et la Dynamique).

440 **References**

- 441 Amiridis, V., Balis, D. S., Giannakaki, E., Stohl, A., Kazadzis, S., Koukouli, M. E. and Zanis, P.: Optical
442 characteristics of biomass burning aerosols over Southeastern Europe determined from UV-Raman lidar
443 measurements, *Atmos. Chem. Phys.*, 9(7), 2431–2440, doi:10.5194/acp-9-2431-2009, 2009.
- 444 Ancellet, G., Pelon, J., Blanchard, Y., Quennehen, B., Bazureau, A., Law, K. S. and Schwarzenboeck, A.:
445 Transport of aerosol to the Arctic: analysis of CALIOP and French aircraft data during the spring 2008
446 POLARCAT campaign, *Atmos. Chem. Phys.*, 14(16), 8235–8254, doi:10.5194/acp-14-8235-2014, 2014.
- 447 Ancellet, G., Pelon, J., Totems, J., Chazette, P., Bazureau, A., Sicard, M., Di Iorio, T., Dulac, F., Mallet, M.,
448 Di Iorio, T., Dulac, F., Mallet, M., Di Iorio, T., Dulac, F. and Mallet, M.: Long-range transport and mixing of
449 aerosol sources during the 2013 North American biomass burning episode: analysis of multiple lidar
450 observations in the western Mediterranean basin, *Atmos. Chem. Phys.*, 16(7), 4725–4742, doi:10.5194/acp-
451 16-4725-2016, 2016.



- 452 Barrie, L. A.: Arctic air pollution: An overview of current knowledge, *Atmos. Environ.*, 20(4), 643–663,
453 doi:10.1016/0004-6981(86)90180-0, 1986.
- 454 Berg, L. K., Gustafson, W. I., Kassianov, E. I. and Deng, L.: Evaluation of a Modified Scheme for Shallow
455 Convection: Implementation of CuP and Case Studies, *Mon. Weather Rev.*, 141(2005), 120810134821004,
456 doi:10.1175/MWR-D-12-00136.1, 2013.
- 457 Blanchard, D. C. and Woodcock, A. H.: The production, concentration, and vertical distribution of the sea-salt
458 aerosols, *Ann. N. Y. Acad. Sci.*, 338(1), 330–347, doi:10.1111/j.1749-6632.1980.tb17130.x, 1980.
- 459 Bodhaine, B. A., Wood, N. B., Dutton, E. G. and Slusser, J. R.: On Rayleigh optical depth calculations, *J. Atmos.*
460 *Ocean. Technol.*, 16(11 PART 2), 1854–1861, doi:10.1175/1520-0426(1999)016<1854:ORODC>2.0.CO;2,
461 1999.
- 462 Breider, T. J., Mickley, L. J., Jacob, D. J., Wang, Q., Fisher, J. A., Chang, R. Y. W. and Alexander, B.: Annual
463 distributions and sources of Arctic aerosol components, aerosol optical depth, and aerosol absorption, *J.*
464 *Geophys. Res.*, 119(7), 4107–4124, doi:10.1002/2013JD020996, 2014.
- 465 Brioude, J., Arnold, D., Stohl, A., Cassiani, M., Morton, D., Seibert, P., Angevine, W., Evan, S., Dingwell, A.,
466 Fast, J. D., Easter, R. C., Pisso, I., Burkhardt, J. and Wotawa, G.: The Lagrangian particle dispersion model
467 FLEXPART-WRF version 3.1, *Geosci. Model Dev.*, 6(6), 1889–1904, doi:10.5194/gmd-6-1889-2013, 2013.
- 468 Brock, C. A., Cozic, J., Bahreini, R., Froyd, K. D., Middlebrook, A. M., McComiskey, A., Brioude, J., Cooper, O.
469 R., Stohl, A., Aikin, K. C., de Gouw, J. A., Fahey, D. W., Ferrare, R. A., Gao, R.-S., Gore, W., Holloway, J.
470 S., Hübler, G., Jefferson, A., Lack, D. A., Lance, S., Moore, R. H., Murphy, D. M., Nenes, A., Novelli, P. C.,
471 Nowak, J. B., Ogren, J. A., Peischl, J., Pierce, R. B., Pilewskie, P., Quinn, P. K., Ryerson, T. B., Schmidt, K.
472 S., Schwarz, J. P., Sodemann, H., Spackman, J. R., Stark, H., Thomson, D. S., Thornberry, T., Veres, P., Watts,
473 L. A., Warneke, C. and Wollny, A. G.: Characteristics, sources, and transport of aerosols measured in spring
474 2008 during the aerosol, radiation, and cloud processes affecting Arctic Climate (ARCPAC) Project, *Atmos.*
475 *Chem. Phys.*, 11(6), 2423–2453, doi:10.5194/acp-11-2423-2011, 2011.
- 476 Burton, S. P., Hair, J. W., Kahnert, M., Ferrare, R. A., Hostetler, C. A., Cook, A. L., Harper, D. B., Berkoff, T. A.,
477 Seaman, S. T., Collins, J. E., Fenn, M. A. and Rogers, R. R.: Observations of the spectral dependence of linear
478 particle depolarization ratio of aerosols using NASA Langley airborne High Spectral Resolution Lidar, *Atmos.*
479 *Chem. Phys.*, 15(23), 13453–13473, doi:10.5194/acp-15-13453-2015, 2015.
- 480 Chazette, P. and Totems, J.: Mini N2-Raman Lidar onboard ultra-light aircraft for aerosol measurements:
481 Demonstration and extrapolation, *Remote Sens.*, 9(12), doi:10.3390/rs9121226, 2017.
- 482 Chazette, P., Marnas, F. and Totems, J.: The mobile Water vapor Aerosol Raman Lidar and its implication in the
483 framework of the HyMeX and ChArMEx programs: application to a dust transport process, *Atmos. Meas.*
484 *Tech.*, 7(6), 1629–1647, doi:10.5194/amt-7-1629-2014, 2014.
- 485 Chazette, P., Totems, J., Ancellet, G., Pelon, J. and Sicard, M.: Temporal consistency of lidar observables during
486 aerosol transport events in the framework of the ChArMEx/ADRIMED campaign at Menorca Island in June
487 2013, *Atmos. Chem. Phys. Discuss.*, 15(22), 32723–32757, doi:10.5194/acpd-15-32723-2015, 2015.
- 488 Chazette, P., Totems, J., Ancellet, G., Pelon, J. and Sicard, M.: Temporal consistency of lidar observations during
489 aerosol transport events in the framework of the ChArMEx/ADRIMED campaign at Minorca in June 2013,
490 *Atmos. Chem. Phys.*, 16(5), 2863–2875, doi:10.5194/acp-16-2863-2016, 2016.
- 491 Chazette, P., Totems, J. and Shang, X.: Atmospheric aerosol variability above the Paris Area during the 2015 heat
492 wave - Comparison with the 2003 and 2006 heat waves, *Atmos. Environ.*, 170, 216–233,
493 doi:10.1016/j.atmosenv.2017.09.055, 2017.
- 494 Chen, F. and Dudhia, J.: Coupling an Advanced Land Surface – Hydrology Model with the Penn State – NCAR
495 MM5 Modeling System . Part I: Model Implementation and Sensitivity, *Mon. Weather Rev.*, 569–585,
496 doi:10.1175/1520-0493(2001)129<0569:caalsh>2.0.co;2, 2001.
- 497 Chu, D. A., Kaufman, Y. J., Ichoku, C., Remer, L. A., Tanré, D. and Holben, B. N.: Validation of MODIS aerosol
498 optical depth retrieval over land, *Geophys. Res. Lett.*, 29(12), 8007, doi:10.1029/2001GL013205, 2002.
- 499 Dee, D. P., Uppala, S. M., Simmons, A. J., Berrisford, P., Poli, P., Kobayashi, S., Andrae, U., Balmaseda, M. A.,
500 Balsamo, G., Bauer, P., Bechtold, P., Beljaars, A. C. M., van de Berg, L., Bidlot, J., Bormann, N., Delsol, C.,
501 Dragani, R., Fuentes, M., Geer, A. J., Haimberger, L., Healy, S. B., Hersbach, H., Hólm, E. V., Isaksen, I.,
502 Kållberg, P., Köhler, M., Matricardi, M., McNally, A. P., Monge-Sanz, B. M., Morcrette, J. J., Park, B. K.,
503 Peubey, C., de Rosnay, P., Tavolato, C., Thépaut, J. N. and Vitart, F.: The ERA-Interim reanalysis:
504 Configuration and performance of the data assimilation system, *Q. J. R. Meteorol. Soc.*, 137(656), 553–597,
505 2011.
- 506 Elvidge, C. D., Zhizhin, M., Baugh, K., Hsu, F. C. and Ghosh, T.: Methods for global survey of natural gas flaring
507 from visible infrared imaging radiometer suite data, *Energies*, 9(1), doi:10.3390/en9010014, 2016.
- 508 Flamant, C., Pelon, J., Chazette, P. and Trouillet, V.: Marine aerosol vertical distribution retrieval using airborne
509 backscatter lidar measurements, *J. Aerosol Sci.*, 29(SUPPL.2), 1998a.
- 510 Flamant, C., Trouillet, V., Chazette, P. and Pelon, J.: Wind speed dependence of atmospheric boundary layer
511 optical properties and ocean surface reflectance as observed by airborne backscatter lidar, *J. Geophys. Res.*



- 512 Ocean., 103(C11), doi:10.1029/98JC02284, 1998b.
- 513 Formenti, P., Boucher, O., Reiner, T., Sprung, D., Andreae, M. O., Wendisch, M., Wex, H., Kindred, D., Tzortziou,
514 M., Vasaras, A. and Zerefos, C.: STAAARTE-MED 1998 summer airborne measurements over the Aegean
515 Sea 2. Aerosol scattering and absorption, and radiative calculations, *J. Geophys. Res.*, 107(D21), 4551,
516 doi:10.1029/2001JD001536, 2002.
- 517 Forster, C., Wandering, U., Wotawa, G., James, P., Mattis, I., Althausen, D., Simmonds, P., O'Doherty, S.,
518 Jennings, S. G., Kleefeld, C., Schneider, J., Trickl, T., Kreipl, S., Jäger, H. and Stohl, A.: Transport of boreal
519 forest fire emissions from Canada to Europe, *J. Geophys. Res.*, 106(D19), 22887, doi:10.1029/2001JD900115,
520 2001.
- 521 Franklin, J. E., Drummond, J. R., Griffin, D., Pierce, J. R., Waugh, D. L., Palmer, P. I., Parrington, M., Lee, J. D.,
522 Lewis, A. C., Rickard, A. R., Taylor, J. W., Allan, J. D., Coe, H., Walker, K. A., Chisholm, L., Duck, T. J.,
523 Hopper, J. T., Blanchard, Y., Gibson, M. D., Curry, K. R., Sakamoto, K. M., Lesins, G., Dan, L., Kliever, J.
524 and Saha, A.: A case study of aerosol scavenging in a biomass burning plume over eastern Canada during the
525 2011 BORTAS field experiment, *Atmos. Chem. Phys.*, 14(16), 8449–8460, doi:10.5194/acp-14-8449-2014,
526 2014.
- 527 Fromm, M., Bevilacqua, R., Servranckx, R., Rosen, J., Thayer, J. P., Herman, J. and Larko, D.: Pyro-
528 cumulonimbus injection of smoke to the stratosphere: Observations and impact of a super blowup in
529 northwestern Canada on 3–4 August 1998, *J. Geophys. Res.*, 110(D8), D08205, doi:10.1029/2004JD005350,
530 2005.
- 531 Hu, S. and Fedorov, A. V.: The extreme El Niño of 2015–2016 and the end of global warming hiatus, *Geophys.*
532 *Res. Lett.*, 44(8), 3816–3824, doi:10.1002/2017GL072908, 2017.
- 533 Iacono, M. J., Delamere, J. S., Mlawer, E. J., Shephard, M. W., Clough, S. A. and Collins, W. D.: Radiative forcing
534 by long-lived greenhouse gases: Calculations with the AER radiative transfer models, *J. Geophys. Res. Atmos.*,
535 113(13), 1–8, doi:10.1029/2008JD009944, 2008.
- 536 IPCC: Climate Change 2014: Impacts, Adaptation, and Vulnerability. Part A: Global and Sectoral Aspects.
537 Contribution of Working Group II to the Fifth Assessment Report of the Intergovernmental Panel on Climate
538 Change, edited by C. B. Field, V. R. Barros, D. J. Dokken, K. J. Mach, M. D. Mastrandrea, T. E. Bilir, M.
539 Chatterjee, K. L. Ebi, Y. O. Estrada, R. C. Genova, B. Girma, E. S. Kissel, A. N. Levy, S. MacCracken, P. R.
540 Mastrandrea, and L. L. White, Cambridge University Press, Cambridge, United Kingdom and New York, NY,
541 USA, UK and New-York, NY, USA., 2014.
- 542 Jacob, D. J., Crawford, J. H., Maring, H., Clarke, A. D., Dibb, J. E., Ferrare, R. A., Hostetler, C. A., Russell, P.
543 B., Singh, H. B., Thompson, A. M., Shaw, G. E., McCauley, E., Pederson, J. R. and Fisher, J. A.: The ARCTAS
544 aircraft mission: design and execution, *Atmos. Chem. Phys. Discuss.*, 9, 17073–17123, doi:10.5194/acpd-9-
545 17073-2009, 2009.
- 546 Janjić, Z. I.: The Step-Mountain Eta Coordinate Model: Further Developments of the Convection, Viscous
547 Sublayer, and Turbulence Closure Schemes, *Mon. Weather Rev.*, 122(5), 927–945, doi:10.1175/1520-
548 0493(1994)122<0927:TSMECM>2.0.CO;2, 1994.
- 549 King, M. D., Kaufman, Y. J., Menzel, W. P. and Tanré, D.: Remote Sensing of Cloud, Aerosol, and Water Vapor
550 Properties from the Moderate Resolution Imaging Spectrometer (MODIS), *IEEE Trans. Geosci. Remote Sens.*,
551 30(1), 2–27, doi:10.1109/36.124212, 1992.
- 552 Kochtubajda, C., Brimelow, J., Flannigan, M., Morrow, B. and Greenhough, M. D.: The extreme 2016 wildfire in
553 fort McMurray, *Bull. Am. Meteorol. Soc.*, 98(8), S176–S177 [online] Available from:
554 [http://content.ebscohost.com/ContentServer.asp?EbscoContent=dGJyMNLe80Sepq84xNvgOLCmr1CeprZSs
555 am4TLaWxWXS&ContentCustomer=dGJyMOzpsE2xp7dJuePfgexy9Yvf5ucA&T=P&P=AN&S=R&D=a9h
556 &K=125041136](http://content.ebscohost.com/ContentServer.asp?EbscoContent=dGJyMNLe80Sepq84xNvgOLCmr1CeprZSs am4TLaWxWXS&ContentCustomer=dGJyMOzpsE2xp7dJuePfgexy9Yvf5ucA&T=P&P=AN&S=R&D=a9h &K=125041136) (Accessed 1 February 2018), 2017.
- 557 Landis, M. S., Edgerton, E. S., White, E. M., Wentworth, G. R., Sullivan, A. P. and Dillner, A. M.: The impact of
558 the 2016 Fort McMurray Horse River Wildfire on ambient air pollution levels in the Athabasca Oil Sands
559 Region, Alberta, Canada, *Sci. Total Environ.*, 618, 1665–1676, doi:10.1016/j.scitotenv.2017.10.008, 2018.
- 560 Law, K. S., Roiger, A., Thomas, J. L., Marelle, L., Raut, J. C., Dalsøren, S., Fuglestedt, J., Tuccella, P., Weinzierl,
561 B. and Schlager, H.: Local Arctic air pollution: Sources and impacts, *Ambio*, 46(s3), 453–463,
562 doi:10.1007/s13280-017-0962-2, 2017.
- 563 Marelle, L., Raut, J.-C., Thomas, J. L., Law, K. S., Quennehen, B., Ancellet, G., Pelon, J., Schwarzenboeck, A.
564 and Fast, J. D.: Transport of anthropogenic and biomass burning aerosols from Europe to the Arctic during
565 spring 2008, *Atmos. Chem. Phys.*, 15(7), 3831–3850, doi:10.5194/acp-15-3831-2015, 2015.
- 566 Marelle, L., Raut, J. C., Law, K. S., Berg, L. K., Fast, J. D., Easter, R. C., Shrivastava, M. and Thomas, J. L.:
567 Improvements to the WRF-Chem 3.5.1 model for quasi-hemispheric simulations of aerosols and ozone in the
568 Arctic, *Geosci. Model Dev.*, 10(10), 3661–3677, doi:10.5194/gmd-10-3661-2017, 2017.
- 569 Morrison, H., Thompson, G. and Tatarskii, V.: Impact of Cloud Microphysics on the Development of Trailing
570 Stratiform Precipitation in a Simulated Squall Line: Comparison of One- and Two-Moment Schemes, *Mon.*
571 *Weather Rev.*, 137(3), 991–1007, doi:10.1175/2008MWR2556.1, 2009.



- 572 Paris, J.-D., Stohl, A., Nédélec, P., Arshinov, M. Y., Panchenko, M. V., Shmargunov, V. P., Law, K. S., Belan, B.
573 D. and Ciais, P.: Wildfire smoke in the Siberian Arctic in summer: source characterization and plume evolution
574 from airborne measurements, *Atmos. Chem. Phys.*, 9(23), 9315–9327, doi:10.5194/acp-9-9315-2009, 2009.
- 575 Peterson, D. A., Hyer, E. J., Campbell, J. R., Fromm, M. D., Hair, J. W., Butler, C. F. and Fenn, M. A.: The 2013
576 Rim Fire: Implications for predicting extreme fire spread, pyroconvection, smoke emissions, *Bull. Am.
577 Meteorol. Soc.*, 96(2), 229–247, doi:10.1175/BAMS-D-14-00060.1, 2015.
- 578 Quennehen, B., Schwarzenboeck, A., Schmale, J., Schneider, J., Sodemann, H., Stohl, A., Ancellet, G.,
579 Crumeyrolle, S. and Law, K. S.: Physical and chemical properties of pollution aerosol particles transported
580 from North America to Greenland as measured during the POLARCAT summer campaign, *Atmos. Chem.
581 Phys.*, 11(21), 10947–10963, doi:10.5194/acp-11-10947-2011, 2011.
- 582 Quinn, P. K., Bates, T. S., Baum, E., Doubleday, N., Fiore, A. M., Flanner, M., Fridlind, A., Garrett, T. J., Koch,
583 D., Menon, S., Shindell, D., Stohl, A. and Warren, S. G.: Short-lived pollutants in the Arctic: their climate
584 impact and possible mitigation strategies, *Atmos. Chem. Phys.*, 8(6), 1723–1735, doi:10.5194/acp-8-1723-
585 2008, 2008.
- 586 Raut, J.-C. and Chazette, P.: Assessment of vertically-resolved PM₁₀ from mobile lidar observations,
587 *Atmos. Chem. Phys.*, 9(21), 2009.
- 588 Raut, J.-C., Marelle, L., Fast, J. D., Thomas, J. L., Weinzierl, B., Law, K. S., Berg, L. K., Roiger, A., Easter, R.
589 C., Heimerl, K., Onishi, T., Delanoë, J. and Schlager, H.: Cross-polar transport and scavenging of Siberian
590 aerosols containing black carbon during the 2012 ACCESS summer campaign, *Atmos. Chem. Phys.*, 17(18),
591 10969–10995, doi:10.5194/acp-17-10969-2017, 2017.
- 592 Rodríguez, E., Toledano, C., Cachorro, V. E., Ortiz, P., Stebel, K., Berjón, A., Blindheim, S., Gausa, M. and de
593 Frutos, A. M.: Aerosol characterization at the sub-Arctic site Andenes (69°N, 16°E), by the analysis of
594 columnar optical properties, *Q. J. R. Meteorol. Soc.*, 138(663), 471–482, doi:10.1002/qj.921, 2012.
- 595 Roiger, A., Thomas, J. L., Schlager, H., Law, K. S., Kim, J., Schäfler, A., Weinzierl, B., Dahlkötter, F., Risch, I.
596 K., Marelle, L., Minikin, A., Raut, J. C., Reiter, A., Rose, M., Scheibe, M., Stock, P., Baumann, R., Bouarar,
597 I., Lerbaux, C. C., George, M., Onishi, T. and Flemming, A. J.: Quantifying emerging local anthropogenic
598 emissions in the arctic region: The access aircraft campaign experiment, *Bull. Am. Meteorol. Soc.*, 96(3), 441–
599 460, doi:10.1175/BAMS-D-13-00169.1, 2015.
- 600 Salmonson, V. V., Barnes, W. L. L., Maymon, P. W. P. W. P. W., Montgomery, H. E. H. E., Ostrow, H.,
601 Salomonson, V. V., Barnes, W. L. L., Maymon, P. W. P. W. P. W., Montgomery, H. E. H. E. and Ostrow, H.:
602 MODIS: Advanced Facility Instrument for Studies of the Earth as a System, *IEEE Trans. Geosci. Remote
603 Sens.*, 27(2), 145–153, doi:10.1109/36.20292, 1989.
- 604 Schmale, J., Schneider, J., Ancellet, G., Quennehen, B., Stohl, A., Sodemann, H., Burkhardt, J. F., Hamburger, T.,
605 Arnold, S. R., Schwarzenboeck, A., Borrmann, S. and Law, K. S.: Source identification and airborne chemical
606 characterisation of aerosol pollution from long-range transport over Greenland during POLARCAT summer
607 campaign 2008, *Atmos. Chem. Phys.*, 11(19), 10097–10123, doi:10.5194/acp-11-10097-2011, 2011.
- 608 Shaw, G. E.: The Arctic Haze Phenomenon, *Bull. Am. Meteorol. Soc.*, 76(12), 2403–2413, doi:10.1175/1520-
609 0477(1995)076<2403:TAHP>2.0.CO;2, 1995.
- 610 Sitnov, S. A. and Mokhov, I. I.: Anomalous transboundary transport of the products of biomass burning from
611 North American wildfires to Northern Eurasia, *Dokl. Earth Sci.*, 475(1), doi:10.1134/S1028334X17070261,
612 2017.
- 613 Skamarock, W., Klemp, J., Dudhia, J., Gill, D., Barker, D., Wang, W., Huang, X. and Duda, M.: A Description of
614 the Advanced Research WRF Version 3., 2008.
- 615 Stohl, A., Forster, C., Frank, A., Seibert, P. and Wotawa, G.: Technical note: The Lagrangian particle dispersion
616 model FLEXPART version 6.2, *Atmos. Chem. Phys.*, 5(9), 2461–2474, doi:10.5194/acp-5-2461-2005, 2005.
- 617 Taylor, J. W., Allan, J. D., Allen, G., Coe, H., Williams, P. I., Flynn, M. J., Le Breton, M., Muller, J. B. A.,
618 Percival, C. J., Oram, D., Forster, G., Lee, J. D., Rickard, A. R., Parrington, M. and Palmer, P. I.: Size-
619 dependent wet removal of black carbon in Canadian biomass burning plumes, *Atmos. Chem. Phys.*, 14(24),
620 13755–13771, doi:10.5194/acp-14-13755-2014, 2014.
- 621 Thomas, J. L., Raut, J.-C., Law, K. S., Marelle, L., Ancellet, G., Ravetta, F., Fast, J. D., Pfister, G., Emmons, L.
622 K., Diskin, G. S., Weinheimer, A., Roiger, A. and Schlager, H.: Pollution transport from North America to
623 Greenland during summer 2008, *Atmos. Chem. Phys.*, 13(7), 3825–3848, doi:10.5194/acp-13-3825-2013,
624 2013.
- 625 Vaughan, G., Draude, A. P., Ricketts, H. M. A., Schultz, D. M., Adam, M., Sugier, J. and Wareing, D. P.: Transport
626 of Canadian forest fire smoke over the UK as observed by lidar, *Atmos. Chem. Phys. Discuss.*, 1–33,
627 doi:10.5194/acp-2017-1181, 2018.
- 628 Warneke, C., Froyd, K. D., Brioude, J., Bahreini, R., Brock, C. A., Cozic, J., De Gouw, J. A., Fahey, D. W.,
629 Ferrare, R., Holloway, J. S., Middlebrook, A. M., Miller, L., Montzka, S., Schwarz, J. P., Sodemann, H.,
630 Spackman, J. R. and Stohl, A.: An important contribution to springtime Arctic aerosol from biomass burning
631 in Russia, *Geophys. Res. Lett.*, 37(1), doi:10.1029/2009GL041816, 2010.



- 632 Winker, D. M., Pelon, J., McCormick, M. P., Pierre, U. and Jussieu, P.: The CALIPSO mission : Spaceborne lidar
633 for observation of aerosols and clouds, Proc. SPIE vol. 4893, 4893, 1–11, doi:10.1117/12.466539, 2003.
634 Winker, D. M., Hunt, W. H. and McGill, M. J.: Initial performance assessment of CALIOP, Geophys. Res. Lett.,
635 34(19), doi:10.1029/2007GL030135, 2007.
636 Yang, Q., Bitz, C. M. and Doherty, S. J.: Offsetting effects of aerosols on Arctic and global climate in the late 20th
637 century, Atmos. Chem. Phys., 14(8), 3969–3975, doi:10.5194/acp-14-3969-2014, 2014.
638